QUATERNARY SLIP RATES AND MOST RECENT SURFACE RUPTURE OF THE BITTERROOT FAULT, WESTERN MONTANA

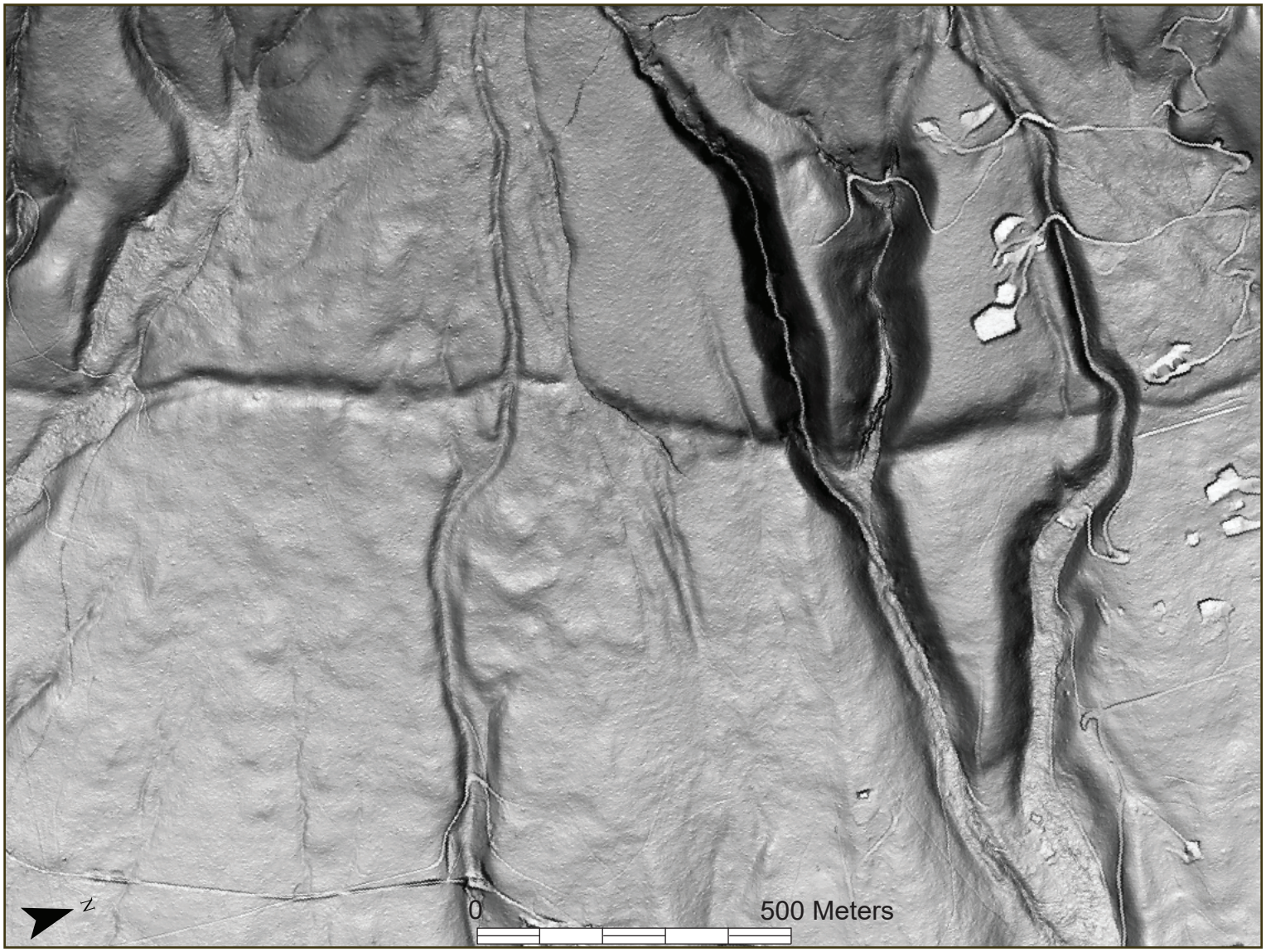

Yann Gavillot,[1] Jeffrey Lonn,[1] Michael Stickney,[1] and Alan Hidy[2]

[1]Montana Bureau of Mines and Geology

[2]Center for Accelerator Mass Spectrometry, Lawrence Livermore National Laboratory

MBMG
Montana Bureau of Mines and Geology

Front photo: Lidar bare-earth slopeshade DEM showing the Bitterroot fault scarp across the Ward Creek fan. Image by Yann Gavillot, MBMG.

QUATERNARY SLIP RATES AND MOST RECENT SURFACE RUPTURE OF THE BITTERROOT FAULT, WESTERN MONTANA

Yann Gavillot,[1] Jeffrey Lonn,[1] Michael Stickney,[1] and Alan Hidy[2]

[1]Montana Bureau of Mines and Geology

[2]Center for Accelerator Mass Spectrometry, Lawrence Livermore National Laboratory

February 2023

Montana Bureau of Mines and Geology Bulletin 142

Montana Bureau of Mines and Geology

TABLE OF CONTENTS

FIGURES

TABLES

ABSTRACT

The Bitterroot fault is a ~100-km-long Quaternary active normal fault that bounds the eastern margin of the north–south-trending Bitterroot Mountains and accommodates extension near the Intermountain Seismic Belt. New detailed mapping using high-resolution topographic data derived from light detection and ranging (lidar) along the southern Bitterroot Range documents multiple generations of fault scarps in Holocene–Pleistocene deposits with vertical offsets that increase in magnitude with age. Fault mapping indicates a complex fault geometry characterized by an *en echelon* pattern of discontinuous segments of 41–78° east-dipping normal faults that appear to cut the older Eocene detachment fault, and locally 70–88° west-dipping antithetic normal faults. ^{10}Be cosmogenic exposure dating provides *in situ* age control for 32 surface boulders (>1 m) sampled in glacial deposits. Near Como Dam, two Pinedale-age glacial moraine sequences yield peak age distributions of 15.0 ± 0.4 ka and 16.4 ± 0.6 ka as apparent exposure ages (e = 0), and 15.4 ± 0.4 ka and 16.8 ± 0.6 ka based on the maximum allowed boulder surface erosion rate (e = 2 mm/ka). Vertical separation of 3.5 ± 0.2 m across the ~16–17 ka glacial moraine offset by the Bitterroot fault scarp yields a fault slip rate of 0.2–0.3 mm/yr. Glacial Lake Missoula highstand shorelines, inset into the ~15 ka glacial moraine and vertically offset 4.6 ± 1.6 m by an antithetic strand of the Bitterroot fault, yield fault slip rates of 0.2–0.5 mm/yr that overlap with fault slip rates on the main strand near Lake Como (0.2–0.3 mm/yr). At the Ward Creek fan located ~15 km to the north of Lake Como, two glacial debris fan sequences yield peak age distributions of 16.6 ± 0.4 ka and 62.8 ± 1.7 ka (e = 0), and 17.0 ± 0.4 ka and 69.9 ± 2.2 ka (e = 2 mm/ka). Vertical separations of 2.4 ± 0.3 m and 4.5 ± 0.2 m on the ~17 ka and ~63–70 ka fan surfaces offset by the Bitterroot fault yield fault slip rates of 0.2–0.3 mm/yr and 0.1 mm/yr, respectively. Our results indicate broadly consistent fault slip rates for the main fault segments at Lake Como (0.2–0.3 mm/yr) and the Ward Creek fan (0.1–0.3 mm/yr) with an along-strike range of 0.1–0.3 mm/yr for the southern Bitterroot fault. Fault scaling relations and evidence of multiple late Quaternary fault surface ruptures suggest the Bitterroot fault could produce a Mw ~7.2 earthquake. Structural model constraints and our slip rate results indicate both high-angle or low-angle fault geometries are possible at depth. A seismogenic low-angle fault model could generate a larger earthquake of Mw >7.2. Earthquake history is unknown for the Bitterroot fault, but fault scarps in young glacial deposits demonstrate its seismogenic potential. Data from this study suggest seismic hazards from the Bitterroot fault may pose a high level of risk to the Missoula metropolitan area, the State's second most populous region, and major infrastructures across the Missoula and Bitterroot Valleys.

INTRODUCTION

Western Montana contains numerous Quaternary faults and is one of the most seismically active regions in the contiguous U.S. (fig. 1), with a history of large, damaging earthquakes (1925, M6.6 Clarkston Valley; 1935, M6.3 and 6.0 Helena; 1947, M6.3 Virginia City; and 1959, M7.3 Hebgen Lake). The Missoula and Bitterroot Valleys are home to over 160,000 people, representing the State's second most populous and rapidly growing regions of Montana, with vital agricultural, water, ecological, and recreational resources. Earthquake ground shaking damage to the Missoula metropolitan area could profoundly affect many communities across Montana and beyond due to sensitive infrastructure, including interstate transportation corridors (rail lines and highways), high-voltage transmission lines that carry power to the Pacific Northwest, telecommunication facilities, fuel and water pipelines, canals, and dams.

Current published hazards models within the National Seismic Hazards Maps (NSHM) show a region of relatively low seismic hazards for the Missoula and Bitterroot Valleys (fig. 1B). However, the Bitterroot fault was not included in the 2018 update of the NSHM (e.g., Petersen and others, 2020), because that earthquake hazard assessment did not integrate results from recent studies on the Bitterroot fault (Stickney and Lonn, 2018; Lonn and Gavillot, 2022; this study). Therefore, the 2018 NSHM underestimates the associated earthquake hazard for the people and infrastructure in the Missoula and Bitterroot Valleys.

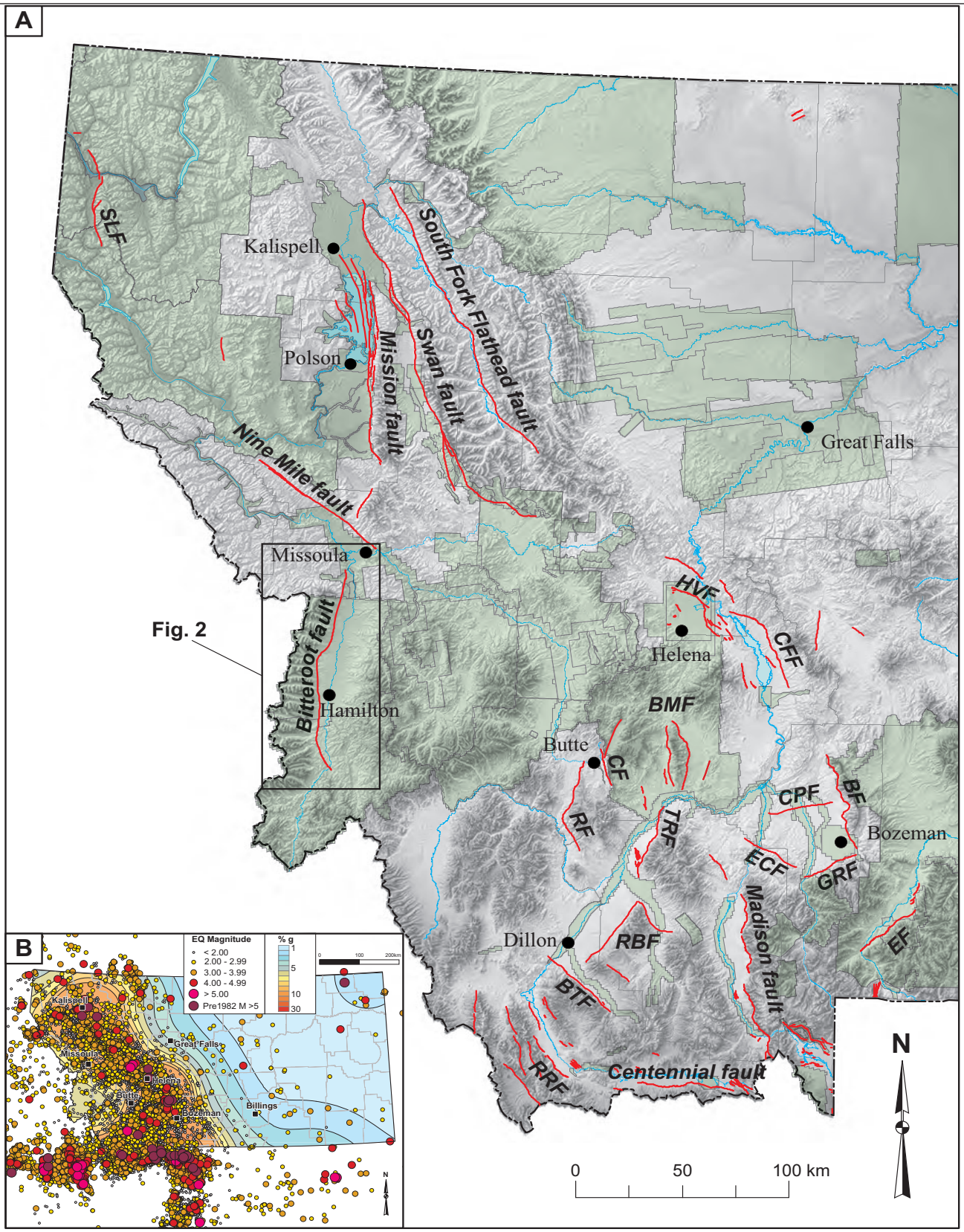

Figure 1. (A) Western Montana map showing inventory of Quaternary faults, including names of major faults. Green shading shows available lidar coverage. Inset box indicates location of figure 2. (B) Seismicity record between 1982 and 2020 from the Montana Regional Seismic Network and Montana seismic hazard map, represented as peak ground acceleration with 10% probability of exceedance in 50 yr. BF, Bridger fault; BMF, Bull Mountain fault system (Bull Mountain western border fault, Whitetail Creek fault, Boulder River valley western border fault); BTF, Blacktail fault; CF, Continental fault; CFF, Canyon Ferry fault; CPF, Central Park fault; ECF, Elk Creek fault; EF, Emigrant fault; GRF, Gallatin Range fault; HVF, Helena Valley fault; RBF, Ruby Range fault system (Ruby Range northern border fault, Ruby Range western border fault); RF, Rocker fault; RRF, Red Rock fault; SLF, Savage Lake fault; TRF, Tobacco Root fault.

The Bitterroot fault is a 100-km-long, east-dipping normal fault that bounds the eastern margin of the north–south-trending Bitterroot Mountains (fig. 2). Recent high-resolution (1 m) digital elevation models derived from light detection and ranging (lidar) data enabled Stickney and Lonn (2018) to map fault scarps cutting late Quaternary surfaces and deposits associated with the Bull Lake (>100 ka) and Pinedale glaciations (~14–22 ka; Pierce, 2004, and references therein; Licciardi and Pierce, 2008, 2018).

Vertical separation and relative age constraints of faulted glacial deposits suggest slip rates are <1 mm/yr. Earthquake history and recurrence interval are unknown for the Bitterroot fault. Length scaling relationships suggest that a single event with a minimum of 2 m surface rupture along the entire length of the Bitterroot fault could produce a Mw ~7.2 earthquake (e.g., Wells and Coppersmith, 1994; Stirling and others, 2013). Fault scarp heights and vertical separation of glacial, periglacial, and alluvial deposits progressively increase with relative age demonstrating that multiple surface-rupturing earthquakes occurred during the Quaternary.

Here we present new detailed mapping using lidar with measurements of deformation, and *in situ* age data from cosmogenic radionuclide (CRN) dating using beryllium-10 (^{10}Be) to constrain Pleistocene–early Holocene fault slip rates of the Bitterroot fault. Our study is located in the southern Bitterroot Valley near Lake Como, an area with well-preserved glacial deposits and geomorphic surfaces deformed by multiple fault scarps (fig. 3). Improved knowledge of the fault slip rates provides new constraints on the late Quaternary fault history and earthquake potential. These new data provide insight on the along- and across-strike variability in fault slip partitioning and extension rates of the Bitterroot fault. Our results support ongoing efforts to update geological parameters and improve regional deformation models used in the NSHM and the USGS Quaternary Fault and Fold Database in the Intermountain West, as well as improving the local earthquake hazards assessment for the Missoula and Bitterroot Valleys. Moreover, this study advances our understanding of the regional tectonics of the Northern Rockies Basin and Range region.

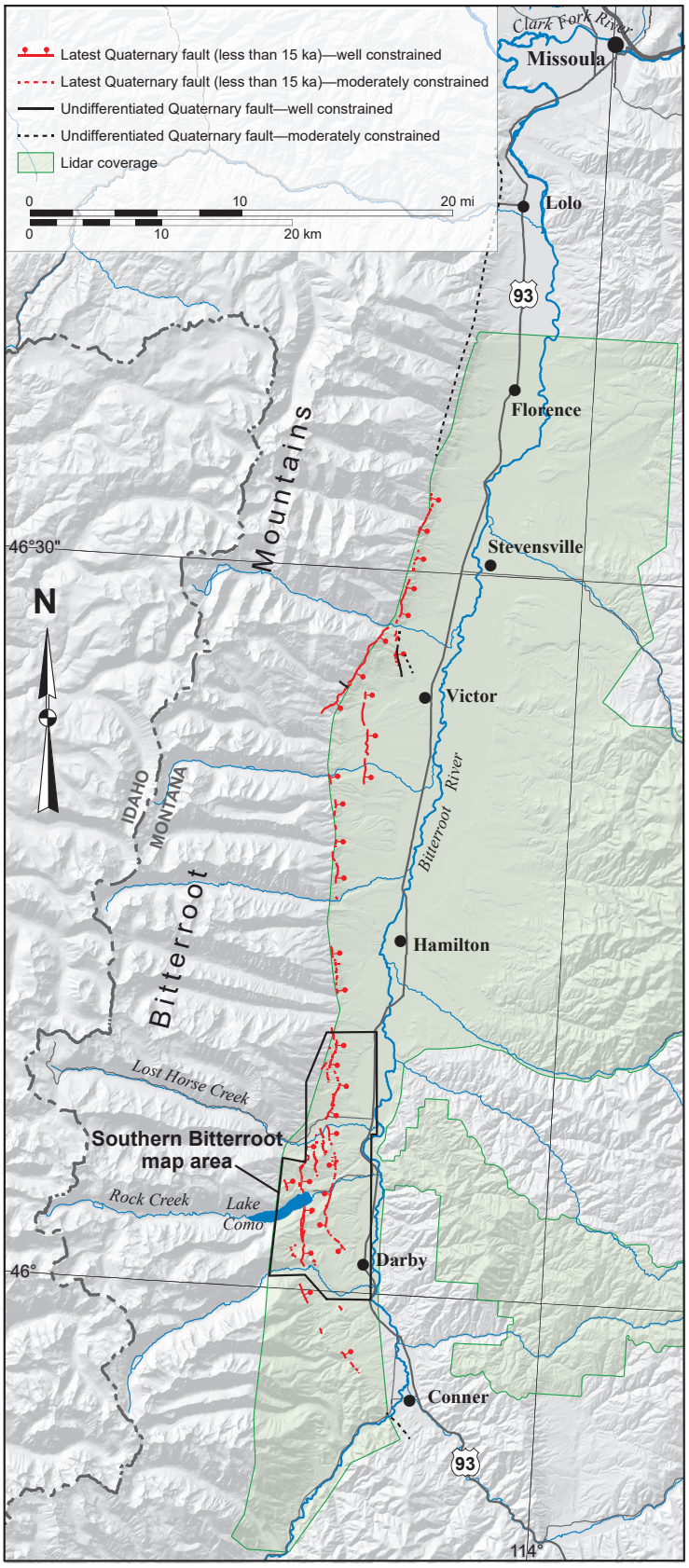

Figure 2. Quaternary fault and location map of the Bitterroot fault and Bitterroot and Missoula Valleys. See figure 1A for location. Base map is 10 m hillshade DEM. Inset box indicates location of new mapping from this study near Lake Como. Northern section of the Southern Bitterroot map area (north of Lost Horse Creek) is revised mapping from Stickney and Lonn (2018).

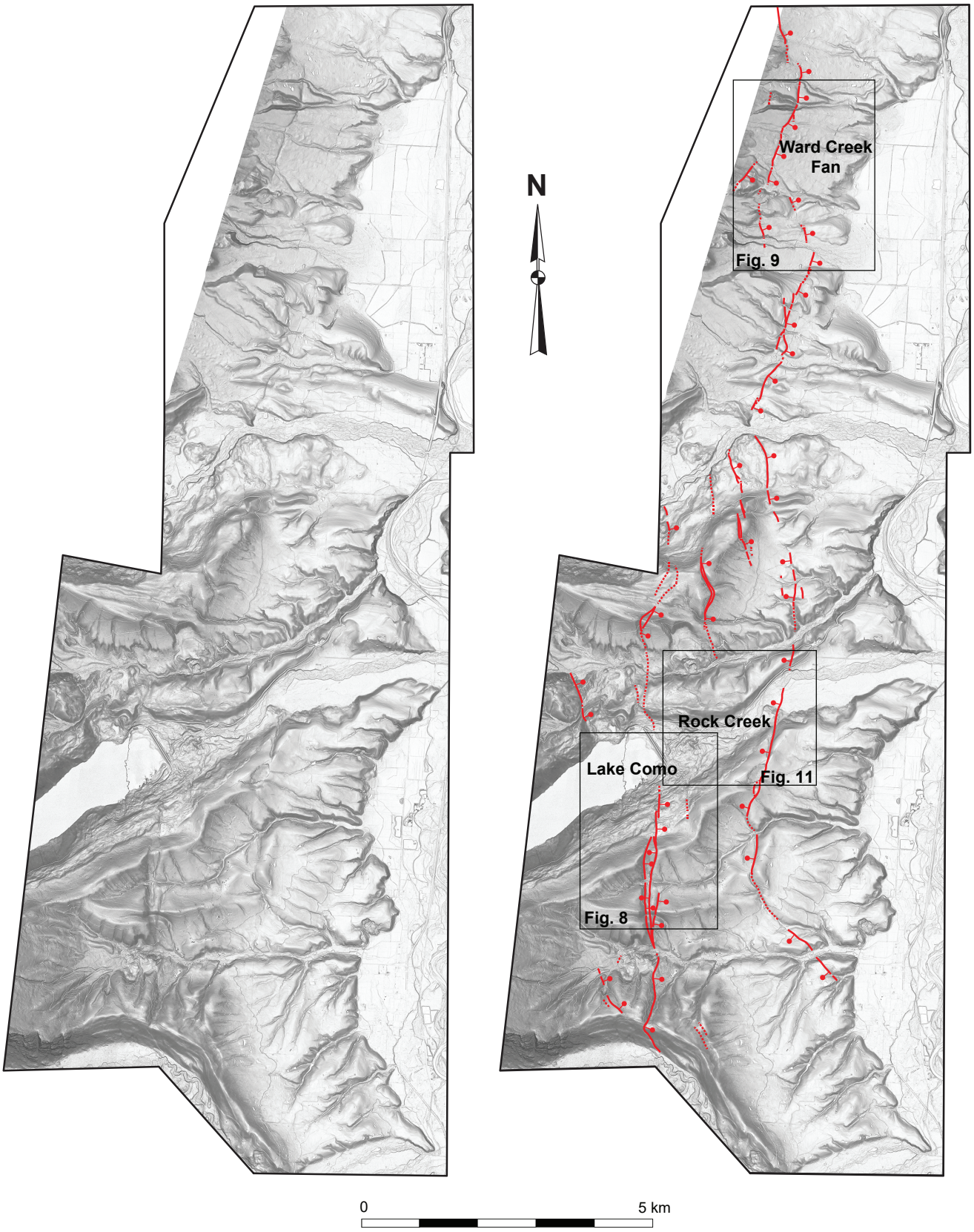

Figure 3. Quaternary fault map of the southern Bitterroot fault. See figure 2 for location. Uninterpreted lidar bare-earth slopeshade DEM shown on the left, and Quaternary fault map with identified fault scarps shown on the right. Red lines are fault traces, dashed where moderately constrained, with ball on the hanging wall indicating normal fault sense of slip. Inset boxes are study sites showing detailed offset geomorphic surfaces and cosmogenic ^{10}Be ages at Lake Como (fig. 8), Ward Creek fan (fig. 9), and Rock Creek study sites (fig. 11).

GEOLOGIC SETTING

The western boundaries of the Bitterroot and Missoula Valleys are defined by the Central Bitterroot Mountains, a N–S-trending mountain range that encompasses the southernmost and tallest sub-range of the Bitterroot Mountains (figs. 1A, 2). The Bitterroot region is located near the western margin of the Intermountain Seismic Belt (ISB), one of the most extensive zones of seismicity within the Continental U.S. (fig. 1B). The ISB is defined as a north–south-oriented 100- to 200- km-wide zone of intraplate seismicity that extends 1,500 km from southern Nevada to northwestern Montana (Smith and Arabasz, 1991; Mason, 1996). In general, the ISB is characterized by diffuse shallow (<20 km) seismicity, Quaternary normal faults, and episodic surface-rupturing earthquakes that accommodate intraplate extensional crustal strain within the western North American plate (Sbar, 1972; Smith and Arabasz, 1991).

The Bitterroot fault is one of the longest Quaternary active faults that accommodates extension in western Montana and the Northern Rockies Basin and Range, as recognized by recent updates to the Quaternary fault database being considered for the 2023 U.S. National Seismic Hazards Model (NSHM; Hatem and others, 2022). Fault geometry is characterized by an ~100-km-long series of fault segments that mark the physiographic boundary between the eastern Bitterroot Mountains range front and the western margin of the Bitterroot Valley (fig. 2). Fault geometry is interpreted as a steeply east-dipping normal fault that cuts the older Eocene Bitterroot detachment (B-detachment) fault, inferred to extend into the subsurface of the Bitterroot Valley (Stickney and Lonn, 2018). Detailed fault mapping indicates a complex fault geometry characterized by *en echelon* patterns of discontinuous fault segments, including west-dipping normal faults that may accommodate part of the total slip budget as half-graben and/or antithetic structures (fig. 2). The degree of slip partitioning, fault activity, and earthquake history among the various segments of the Bitterroot fault is unclear.

Earthquake frequency and Quaternary fault activity for the Bitterroot fault are poorly constrained when compared with other active ISB structures. The 1959 M7.3 Hebgen Lake earthquake (Witkind and others, 1962; Witkind, 1964; Myers and Hamilton, 1964) ruptured multiple normal faults and is the only historic surface-rupturing earthquake in southwest Montana. The Hebgen Lake earthquake was one of the largest continental normal faulting events in recorded history. It produced extensive multi-segment surface ruptures for >10 km with fault scarp heights of 4–6 m and a major landslide that dammed the Madison River. This widely felt event caused 29 fatalities, but predates the major infrastructure and population growth across western Montana over the past 60 yr.

Notably, the Bitterroot fault was not included in the 2018 version of the Montana seismic hazard map or USGS National Hazards Seismic Model (fig. 1B). This omission was attributed to the lack of available slip rate and earthquake recurrence data. Limited constraints of Quaternary fault activity and lack of paleoseismic data for the Bitterroot fault underscore the importance of new and improved constraints of Holocene–Pleistocene fault deformation rates and earthquake history. Recent updates to the Quaternary faults database that underlies the 2023 NSHM (Hatem and others, 2022) now include the Bitterroot fault from Stickney and Lonn (2018), but will not include the results from this study until subsequent NSHM updates.

No previous quantitative slip rates exist for the Bitterroot fault. This study provides a new dataset of numerical ages that constrain late Quaternary slip rates based on five faulted geomorphic surfaces within three study sites (Lake Como, Ward Creek, and Rock Creek areas) using ^{10}Be cosmogenic radionuclide dating (fig. 3).

QUATERNARY MAPPING OF THE BITTERROOT FAULT

The Bitterroot fault is broadly categorized as a continuous N–S-trending normal fault with Quaternary activity that extends for ~100 km along the Bitterroot Mountains range front (fig. 1A). This fault system extends northward along the range front, from at least the town of Darby in the south to at least the town of Lolo in the north (fig. 2). Recent geologic mapping and geomorphic interpretation of lidar data (Stickney and Lonn, 2018; Lonn and Gavillot, 2022; this study) revealed a more complex fault system along its mapped trace characterized by along-strike variability and multiple discontinuous fault segments (figs. 2, 3). Just north of the latitude of Victor, the northern section of the Bitterroot fault is defined as a single NNE–

SSW-trending east-dipping fault trace. Farther south, between Victor and Hamilton, the central section of the Bitterroot fault consists of one, and in places two, parallel east-dipping N–S-trending fault traces. South of Hamilton, the southern section of the Bitterroot fault consists of numerous parallel *en echelon* fault traces trending N–S to NW–SE, east- and west-dipping faults, and local fault grabens (figs. 2, 3).

This study produced an updated, more detailed Quaternary fault map (fig. 3) and a new 1:24,000-scale geologic map (fig. 4; Lonn and Gavillot, 2022) in the Southern Bitterroot area near Lake Como (see fig. 2 for location). The mapped area encompasses 118 km^2 and builds on previous work in the Bitterroot Valley by Lonn and Sears (2001) and Stickney and Lonn (2018).

Field observations combined with topographic and remote sensing analyses using lidar data identified numerous fault scarps in Pleistocene–Holocene deposits (figs. 3–7). Fault scarps associated with the Bitterroot fault occur within various Quaternary surficial deposits, but locally scarps also juxtapose Eocene–Cretaceous granitic rocks in its footwall (granodiorite with mylonitic and fault breccia zones; TKg) against Quaternary deposits in its hanging wall (figs. 3, 4). Foliated bedrock that includes the Bitterroot mylonite (TKg) dips 10–43°SE, with an average of ~20°SE, and is associated with the older deformation history of the Eocene B-detachment fault. The gently dipping B-detachment is vertically separated and cut at the surface by the Quaternary slip along the steeply dipping Bitterroot fault (figs. 4, 5). Previous maps (Berg and Lonn, 1996; Lonn and Berg, 1996; Lonn and Sears, 2001) show similar patterns along the Bitterroot range front.

Map relations, fault dip calculations using 3-point problem methods, field observations, topographic data, and cross-section constraints indicate the main trace of the Bitterroot fault is a 41–78° east-dipping normal fault (figs. 3–7; appendix B). East of Lake Como and the main fault trace, mapping and fault dip calculations indicate an approximately 10-km-long, 70–88° west-dipping normal fault interpreted as an antithetic structure to the main strand of the east-dipping Bitterroot fault (figs. 3–7; appendix B).

Subsurface fault models constrained by cross-section interpretation provide two permissible structural solutions for the Bitterroot fault as a high-angle or low-angle seismogenic normal fault (fig. 5). Deeper fault geometry of the Bitterroot fault could either cut the B-detachment and remain as a steeply dipping fault (fig. 5A), or alternatively merge with preexisting structural weaknesses in the ~1-km-thick mylonitic fabric of the B-detachment as a seismogenic, low-angle fault (fig. 5B). Our mapping and cross sections indicate either fault model is possible; both models have implications for the seismogenic fault width and associated seismic hazards of the Bitterroot fault (see discussion on earthquake potential).

Quaternary–Tertiary gravels (QTgc) with erosional contacts and angular unconformities overlie the B-detachment and west-tilted Eocene volcanics (Tv) exposed along the Bitterroot River (figs. 4, 5). Map relations and cross-sections indicate up to ~500–600 m of Quaternary–Tertiary gravels (see Lonn and Gavillot, 2022, for more detail), consistent with correlative deposits thickening northward in the Bitterroot Valley. These gravels are displaced by Quaternary movement along the Bitterroot fault (figs. 6, 7). However, cross-section constraints do not suggest significant syn-orogenic growth associated with the Bitterroot fault (fig. 5). Various glacial, fluvial/alluvial, and landslide deposits, ranging in thickness from 1 to 120 m, stratigraphically overlie the Quaternary–Tertiary gravels (see Lonn and Gavillot, 2022, for more detail). These Quaternary units mapped across the Bitterroot fault demonstrate surface deformation with vertical separation across fault scarps that increase with relative age (figs. 3–7).

PRE-QUATERNARY BITTERROOT FAULT HISTORY

The core of the Bitterroot Mountains is composed of a well-studied Eocene metamorphic core complex (e.g., Hyndman, 1980; Foster and others, 2001). Cretaceous to Eocene intrusive rocks mainly underlie the Bitterroot Mountains in the footwall of the B-detachment, which experienced exhumation between 53 and 30 Ma (Foster and Raza, 2002). The gently east-dipping Eocene B-detachment (figs. 4, 5) was responsible for the rapid exhumation of these mid-crustal rocks from depths of >20 km (Foster and others, 2001). This fault exhibits a transition from amphibolite facies gneiss containing mylonitic bands to greenschist facies shearing to brittle faulting through time as structural levels became increasingly shallow.

The hanging wall of the B-detachment is composed mainly of Mesoproterozoic metasedimentary rocks (YXm) intruded by Cretaceous to Eocene granitic rocks (TKg). Tertiary volcanic rocks (Tv) unconformably and discontinuously overlie the metamorphic–plutonic bedrock (figs. 4, 5). The age of the Tertiary volcanic unit is unknown but inferred to be Eocene and associated with extension on the B-detachment (Berg and Lonn, 1996). In the few places where hanging wall rocks are preserved near the B-detachment along the Bitterroot range front, they are extensively brecciated, in contrast to the gneissic and mylonitized footwall rocks. The trace of the B-detachment fault is shown approximately at the contact between the amphibolite facies mylonitic gneiss, shown by mylonitic foliation/lineation symbols, and the brecciated rocks. The trace of the B-detachment is exposed discontinuously along and east of the mountain front (fig. 4).

Foster and Raza (2002) postulated that steep east-dipping normal faults in the Bitterroot Valley, including the Bitterroot fault, are Miocene in age and responsible for the uplift and exposure of the older Eocene B-detachment fault (figs. 4, 5). Stickney and Lonn (2018) postulated that erosion removed most of the brecciated and less resistant rocks of the B-detachment hanging wall, leaving the resistant gneiss of the footwall to form the planar, gently sloping Bitterroot Mountain front. However, the lack of AFT cooling ages and exhumation younger than ~22 Ma along the range front (Foster and Raza, 2002) suggest no rapid exhumation or significant uplift has occurred on the Bitterroot fault since early Miocene. Shallow sloping range front facets (<20–30°) and modest topographic gradients across the mapped Quaternary faults in the Bitterroot Valley (figs. 6A, 7C, 7E) suggest the Bitterroot fault is an incipient structure with a landscape primarily controlled by the older B-detachment fault history. Estimates of total fault displacement recorded in the vertical separation (~200–500 m) of the basal Quaternary–Tertiary gravels (QTgc) are consistent with the interpretation of a young (Late Miocene to Plio/Pleistocene) onset for the Bitterroot fault (fig. 5). The Bitterroot fault may represent the modern expression of the Basin-and-Range-style extension in the Northern Rockies as a high-angle normal fault (fig. 5A). Alternatively, the Quaternary Bitterroot fault may represent a low-angle fault controlled at depth by the structural inheritance of the gently dipping Bitterroot detachment mylonitic gneiss (fig. 5B).

LATE CENOZOIC–QUATERNARY MAP UNITS

Quaternary–Tertiary Gravels

Exhumation and erosional history of the Bitterroot Mountains post-dating the B-detachment are recorded in the unconsolidated Cenozoic deposits (unit QTgc). These deposits accumulated in the Bitterroot Valley to depths as great as ~700–1,000 m based on well logs and gravity model constraints north of Hamilton (Norbeck, 1980; Smith, 2006; fig. 2). Our maximum estimate of a ~500- to 600-m-thick Quaternary–Tertiary gravel assemblage in the southern Bitterroot map areas is consistent with a northward thickening of correlative Cenozoic sediments and widening of the Bitterroot Valley. Fossils recovered from QTgc deposits range in age from Oligocene to Pliocene(?) (Konizeski, 1958; McMurtrey and others, 1972; Dale Hanson, Museum of the Rockies, written commun., 2018). Unit QTgc is a sandy, well-sorted, pebble–cobble conglomerate containing rounded clasts dominantly of Mesoproterozoic Belt Supergroup quartzite (Lonn and others, 2020), and lesser amounts of mylonitic gneiss, granite, volcanic rocks, and other metamorphic rocks. These gravels are interbedded with tuffaceous silt and clay intervals that may represent floodplain deposits. Because the clasts represent lithologies present in the entire Bitterroot River Basin, Lonn and Sears (2001) interpreted QTgc as a fluvial deposit deposited by an ancestral Bitterroot River (McMurtrey and others, 1972; Lonn and Sears, 2001). Larger and more angular clasts occur near the eastern and western valley margins and appear to interfinger with and grade into the fluvial deposits; the angular clasts probably represent debris-flow deposits shed from the surrounding mountains. In the map area, quartzite-dominated gravels grade upward to granite/mylonitic-gneiss-dominated gravels near the top of QTgc (fig. 6C). These granitic/gneissic clasts may be glaciofluvial and therefore Quaternary. QTgc was deposited unconformably on the underlying YXm, TKg, and Tv units, which formed an irregular paleosurface with considerable relief. In most places the upper QTgc contact is an erosional pediment surface with a minimum age constrained only by the overlying Pleistocene glacial deposits. The existence of glacial till underlying the pediment surface north of Hayes Creek suggests that at least some pediment surfaces developed in the Quaternary.

Map Units

- Qal — Stream alluvium (Holocene and Late Pleistocene)
- Qpa — Paludal deposit (Holocene)
- Qaf — Alluvial fan and debris-flow deposits (Holocene and Late Pleistocene)
- Qls — Landslide and earthflow deposits (Holocene and late Pleistocene)
- Qatd — Alluvium of the Darby terrace (late Pleistocene?)
- Qatr — Alluvium of the Riverside terrace (late Pleistocene?)
- Qath — Alluvium of the Hamilton terrace (late Pleistocene?)
- Qgto/to — Younger glacial outwash deposits and older glacial till deposits, undivided (Pleistocene)
- Qgoy — Younger glacial outwash deposits (latest Pleistocene to early Holocene)
- Qgty — Younger glacial till deposits (late Pleistocene)
- Qdfy — Younger glacial debris flow deposits (latest Pleistocene to early Holocene)
- Qgom — Middle-aged glacial outwash deposits (Pleistocene)
- Qgtm — Middle-aged glacial till deposits (Pleistocene)
- Qdfm — Middle-aged glacial debris flow deposits (late Pleistocene)
- Qgoo — Older glacial outwash deposits (Pleistocene)
- Qgto — Older glacial till deposits (Pleistocene)
- Qdfo — Older glacial debris flow deposits (Pleistocene)
- QTgc — Gravel and clay of the ancestral Bitterroot River deposits (Oligocene to Plio-Pleistocene?)
- Tv — Volcanic rocks (Paleocene to Miocene?)
- TKg — Foliated granodiorite and unfoliated granite, undivided (Cretaceous and Eocene)
- YXm — Metamorphic rocks (Proterozoic)

MAP SYMBOLS

- Contact: dashed where approximately located
- Fault: dashed where approximately located
- Detachment fault: hachures on upper plate; dashed where approximately located
- Scarp on fault: dashed where approximately located; hachures point downscarp
- Inclined metamorphic or tectonic foliation: showing strike and dip
- Approximate plunge direction of inclined lineation
- Cosmogenic radionuclide sample location
- Shoreline
- Glacial Moraine Crest
- 4230' — Glacial Lake Missoula Maximum Elevation
- Breccia

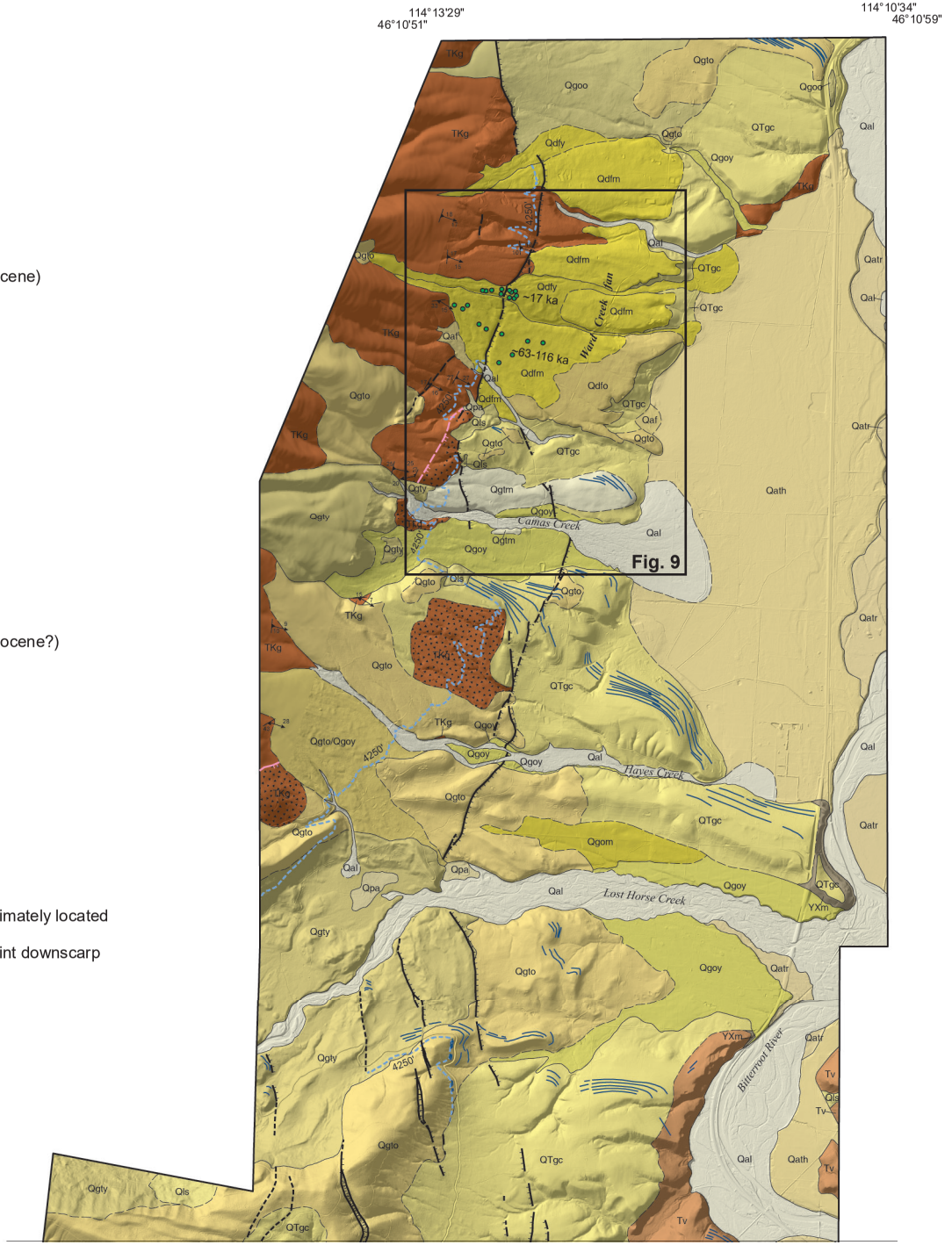

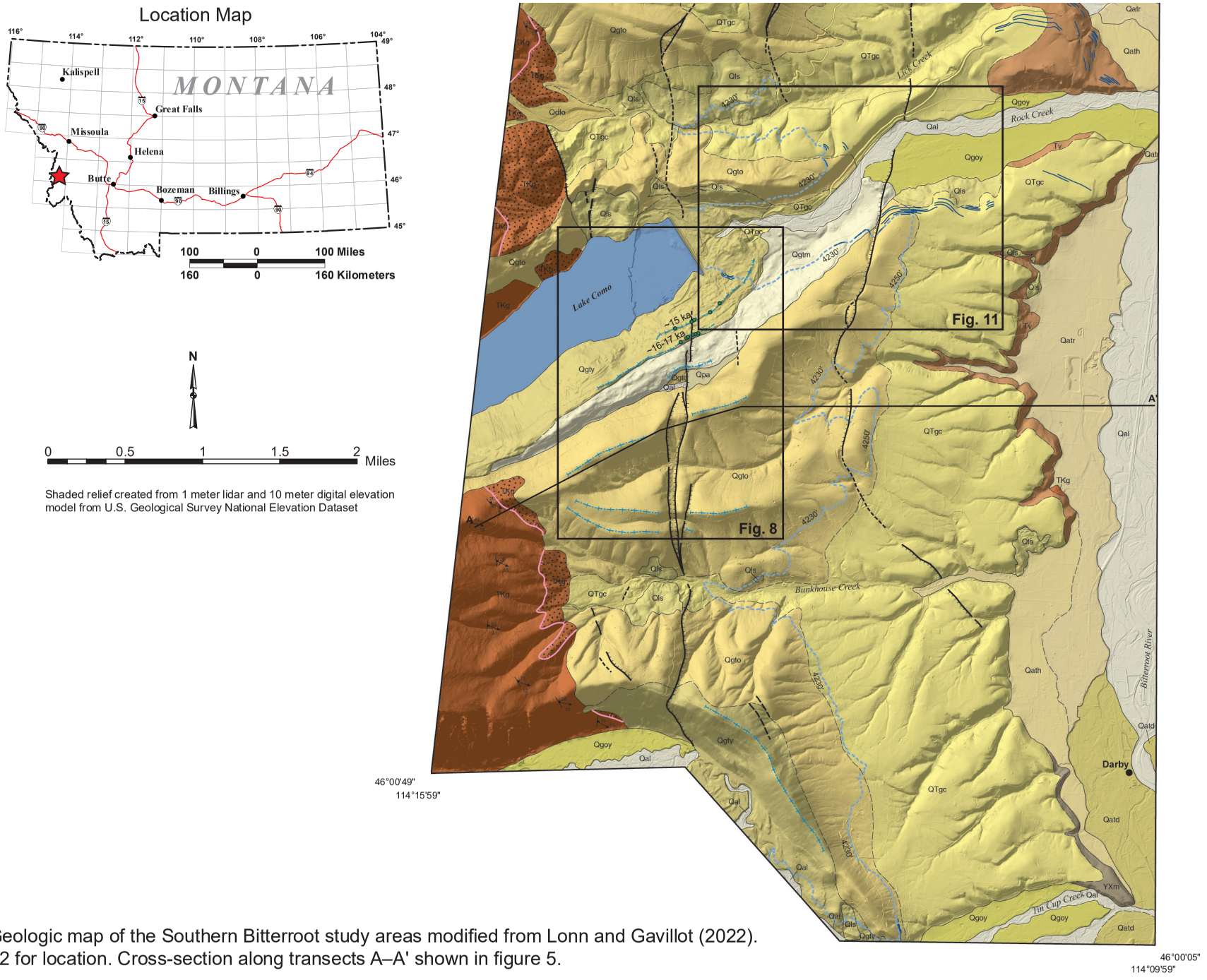

Figure 4. Geologic map of the Southern Bitterroot study areas modified from Lonn and Gavillot (2022). See figure 2 for location. Cross-section along transects A–A' shown in figure 5.

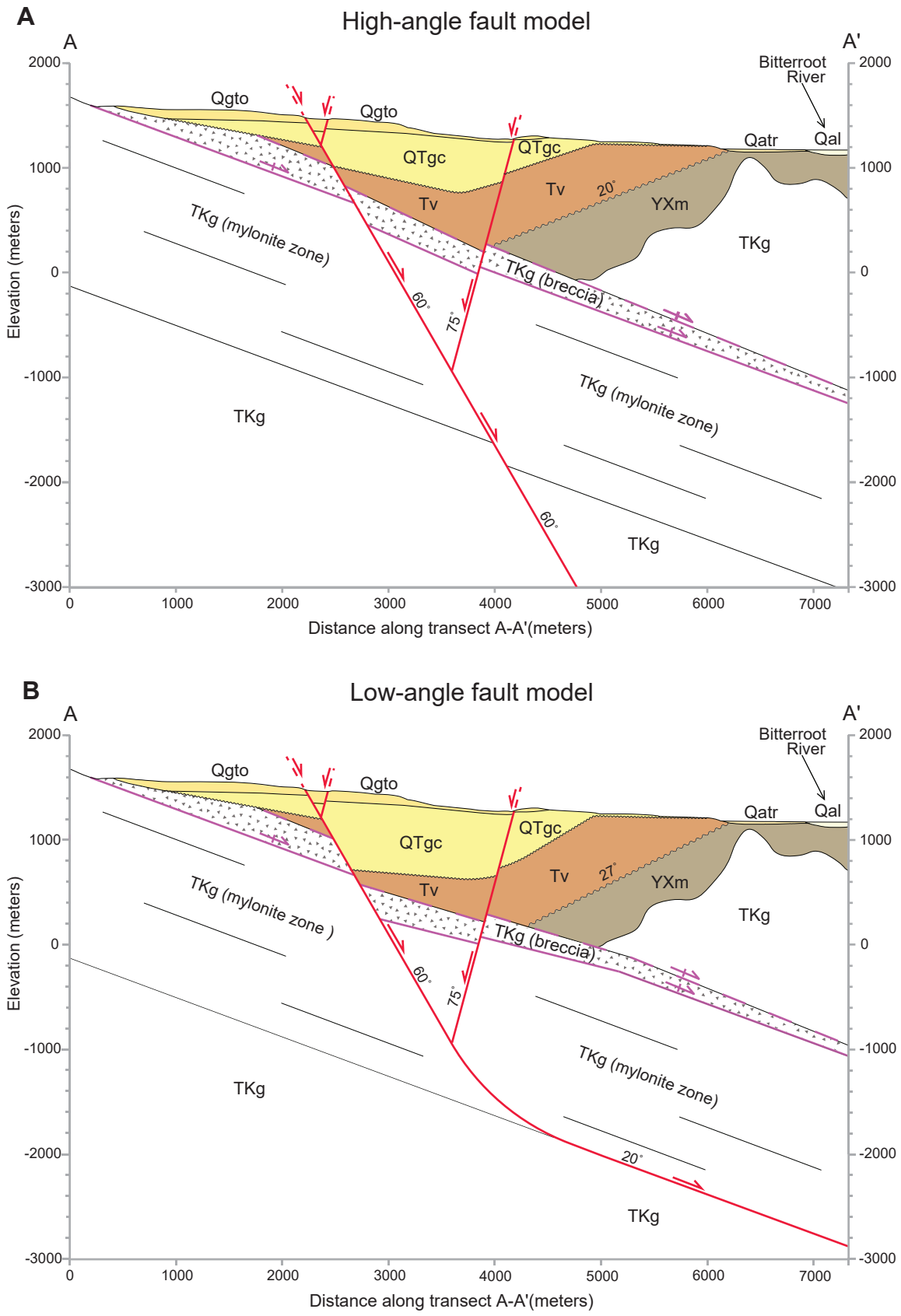

Figure 5. Structural cross-sections of the Bitterroot fault along transect A–A' showing two viable subsurface fault models that restore to the same pre-Bitterroot fault geometry: (A) high-angle fault model; (B) low-angle fault model. See figure 4 for transect location.

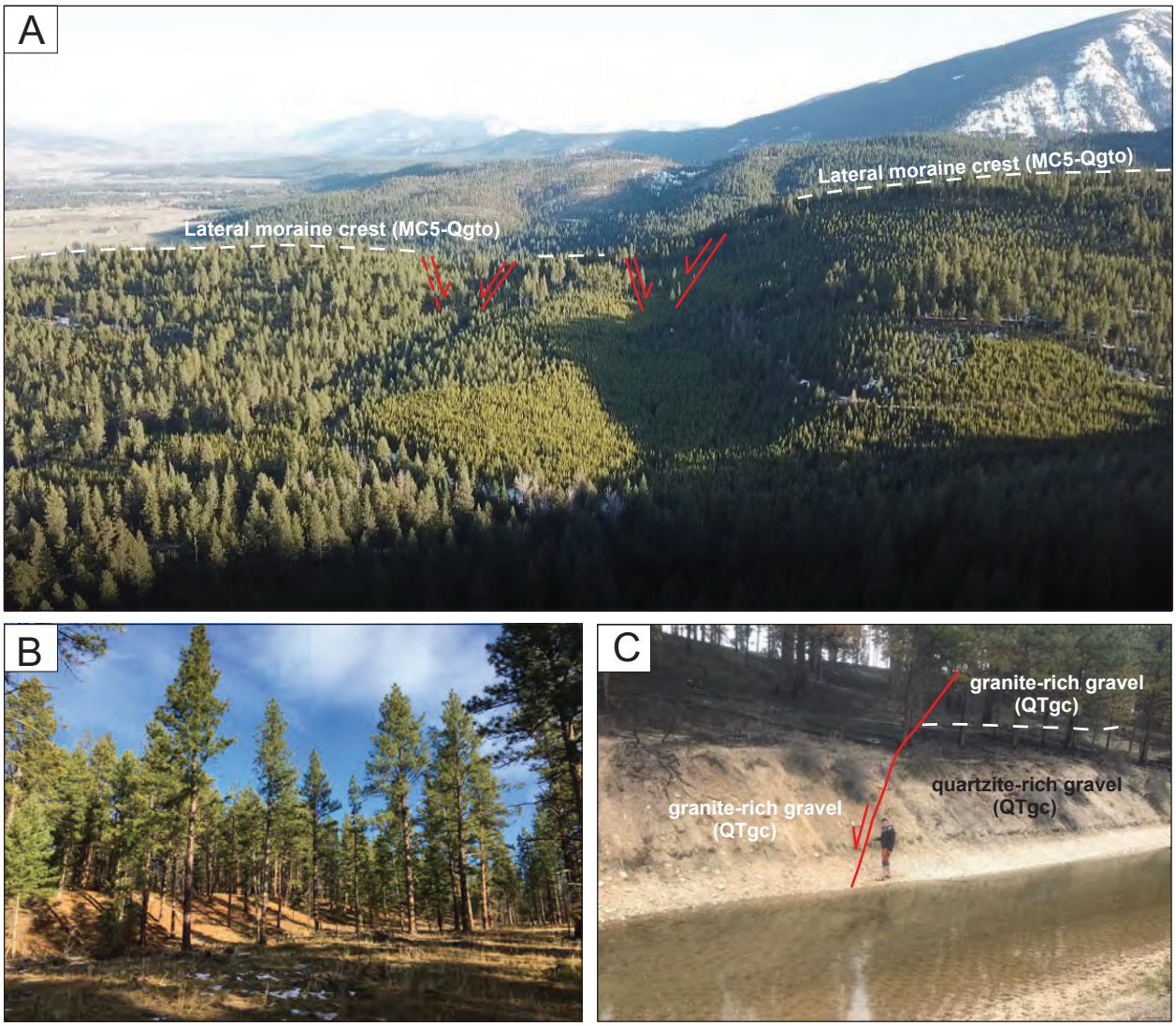

Figure 6. Field photos of Bitterroot fault scarps. (A) Aerial drone view to the south showing in the background gentle (~20–30°) east-sloping range front of the Bitterroot Mountains controlled by the B-detachment mylonite, and in the foreground the high-angle fault scarps that offset old glacial moraine deposits (Qgto) with a fault scarp height of ~75 m. (B) View to the NW of well-exposed ~10-m-high fault scarp offsetting S2 (Qdfm), a middle-aged (older than Pinedale) glacial debris fan surface at the Ward Creek fan. (C) View to the NE of an outcrop exposure of the west-dipping antithetic fault near Rock Creek truncating deposits within the Quaternary–Tertiary gravels (QTgc).

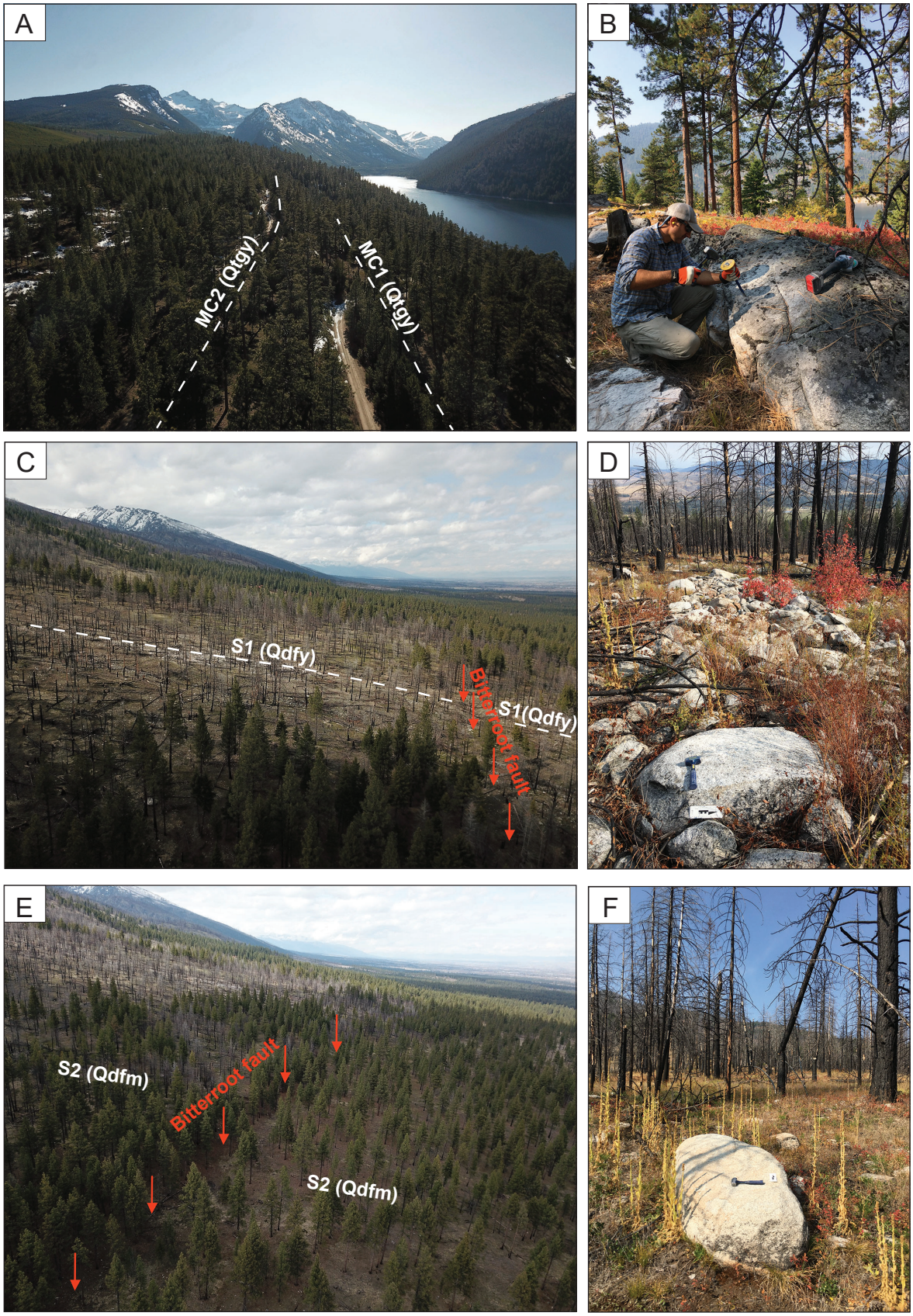

Figure 7. Field photos of geomorphic surfaces with boulders sampled for cosmogenic ^{10}Be dating. (A) Aerial drone view to the west showing the young Pinedale-age glacial lateral moraines (MC1–MC2) sourced from Rock Creek Glacier. Como Lake is visible at right. (B) Example of boulder sampled for age dating along moraine crest near Lake Como. (C and E) Aerial drone views to the north showing the young (S1) and middle-aged (S2) glacial debris fans at the Ward Creek fan site displaced by the Bitterroot fault. (D and F) Examples of debris flows surface morphology and boulder fields sampled for age dating on surface S1 (D) and S2 (F).

Quaternary Deposits

Older glacial outwash (Qgoo) and glacial debris fans (Qdfo) are eroded into and mantle the relict pediment surfaces, and are associated with older glacial till (Qgto) deposited at high levels downstream from the mouths of the Bitterroot Mountains canyons. Weber (1972) postulated that these older glacial deposits represent at least two different glacial stages. Our mapping supports his theory, recognizing three lateral moraine crests within Qgto south of Lake Como (fig. 4). Field observations (smooth and inflated surfaces) and topographic positions suggest these glacial moraines represent Bull Lake or older glaciation (>100 ka; Pierce, 2004, and references therein; Liccardi and Pierce, 2008).

Younger glacial deposits (Qgom, Qgoy, Qgtm, Qgty, Qdfm, Qdfy) occur between and topographically below incised remnants of the older glacial deposits. These young glacial moraines are characterized by hummocky surfaces and fresh boulder fields, which correlate at lower elevations to glacial outwash terraces preserved along modern stream margins. These young glacial deposits are interpreted to represent Pinedale Glaciation (~15–20 ka; Pierce, 2004, and references therein; Liccardi and Pierce, 2008).

No *in situ* age data existed prior to this study for any of the alpine glacial deposits in the Bitterroot Mountains or western Montana. Relative age chronology and mapping of these glacial deposits were based on limited data of Pleistocene glaciation from various sites in the Rocky Mountains.

QUATERNARY GEOCHRONOLOGY

Methods

We employed ^{10}Be cosmogenic radionuclide (CRN) dating of geomorphic surfaces to constrain the exposure ages of glacial moraines at the Lake Como study site (fig. 8) and glacial debris fans at the Ward Creek study site (fig. 9). Surface exposure dates are established using ^{10}Be isotopes from the quartz-rich bedrock or sediments (e.g., Gosse and Phillips, 2001; Frankel and others, 2007). We targeted surface boulders >1 m in diameter sourced from the Eocene–Cretaceous foliated granodiorite and mylonite bedrock (TKg) and collected the uppermost centimeter of the boulder surface with a battery-powered angle gridder with a diamond blade, hand chisel, and hammer (figs. 7B, 7D, 7F). Each sampling interval was confined to a 1 ± 0.5-cm-thick sampling horizon. A minimum of five to six boulders were sampled from each geomorphic surface that extend 250–750 m in length and are nearly perpendicular in orientation across fault scarps. We avoided sampling boulders that displayed potential evidence of post-exposure modification such as spallation, uneven weathering, lack of glacial abrasion surfaces, tree uprooting, soil deflation, and anthropogenic activity.

Samples were physically separated (crushed, sieved to 250–500 μm, and magnetic minerals removed via Frantz magnetic separation) at the Montana Bureau of Mines and Geology (MBMG), and then sent to the Center for Accelerator Mass Spectrometry (CAMS), Lawrence Livermore National Lab (LLNL), for further quartz purification, chemical processing, and analysis of ^{10}Be via accelerator mass spectrometry (AMS). Beryllium (^{10}Be) concentrations from quartz separated from each amalgamated boulder surface rock chip followed methods given in Kohl and Nishiizumi (1992) and Licciardi (2000). The CAMS 10-MV model FN tandem Van de Graaf accelerator configured with post-stripping for isobaric ^{10}Be (Hidy and others, 2018) was used to measure ^{10}Be/^{9}Be isotopic ratios. Following Be extraction procedures (Ditchburn and Whitehead, 1994), isotopic ratio measurements, and ^{10}Be concentration calculations, we used the CRONUS Age Calculator from Balco and others (2008) to provide the exposure age models for each sample. This approach yielded surface ages that account for post-depositional exposure and erosion (table 1; appendix A). Age models include measured density constraints of sampled boulder deposits of 2.6 ± 0.1 g/cm^3 for bedrock foliated granodiorite and mylonite boulders. Exposure ages for each surface sample were calculated using version 3 of the CRONUS online calculator (Balco and others, 2008). The "topographic and shielding" calculator was used to calculate sample-specific topographic shielding factors based on field measurements of horizon and surface orientations, which we included in the full CRONUS code data input (appendix A). The default scaling scheme of Lal (1991) and Stone (2000) was used for estimating site production rates. To test the sensitivity of our ages to erosion rates, we ran the code data input with two end-member scenarios, e = 0 and e = 2mm/ka, which provided minimum and maximum ages, respec-

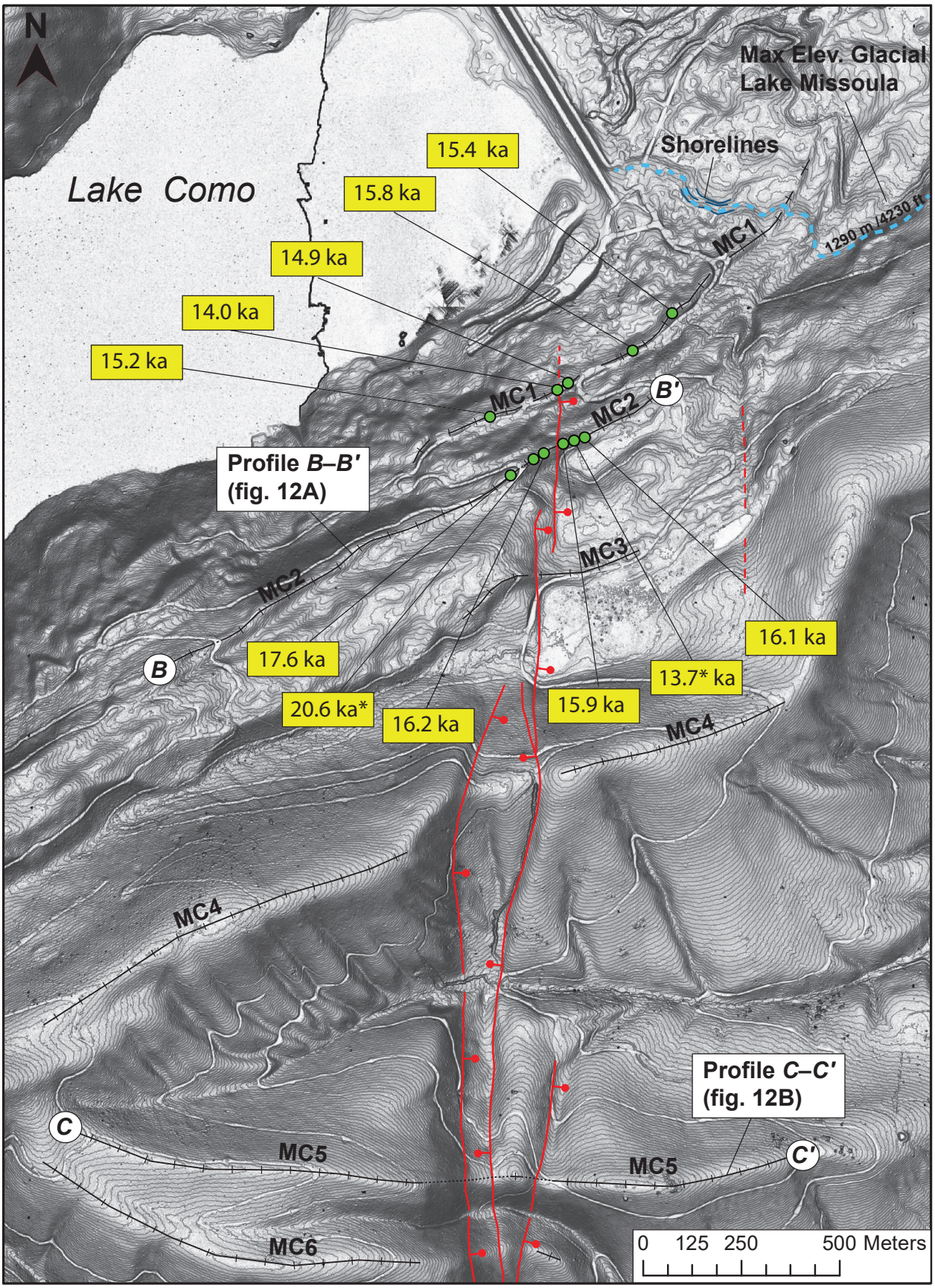

Figure 8. Detailed map of the Bitterroot fault scarps and moraine crests MC1–MC6 south of Lake Como showing cosmogenic ^{10}Be ages results from sampled boulders. Base map is lidar slopeshade DEM with 2 m contour interval. See figure 3 for location and table 1 for age results. MC1–MC2, Young Pinedale moraine crests in glacial till (Qgty); MC3, middle-aged moraine crest in glacial till (Qgtm); MC4–MC6, Old Bull Lake(?) moraine crests in glacial till (Qgto). *Ages identified as outliers based on probability density plots age models (figs. 10A, 10B).

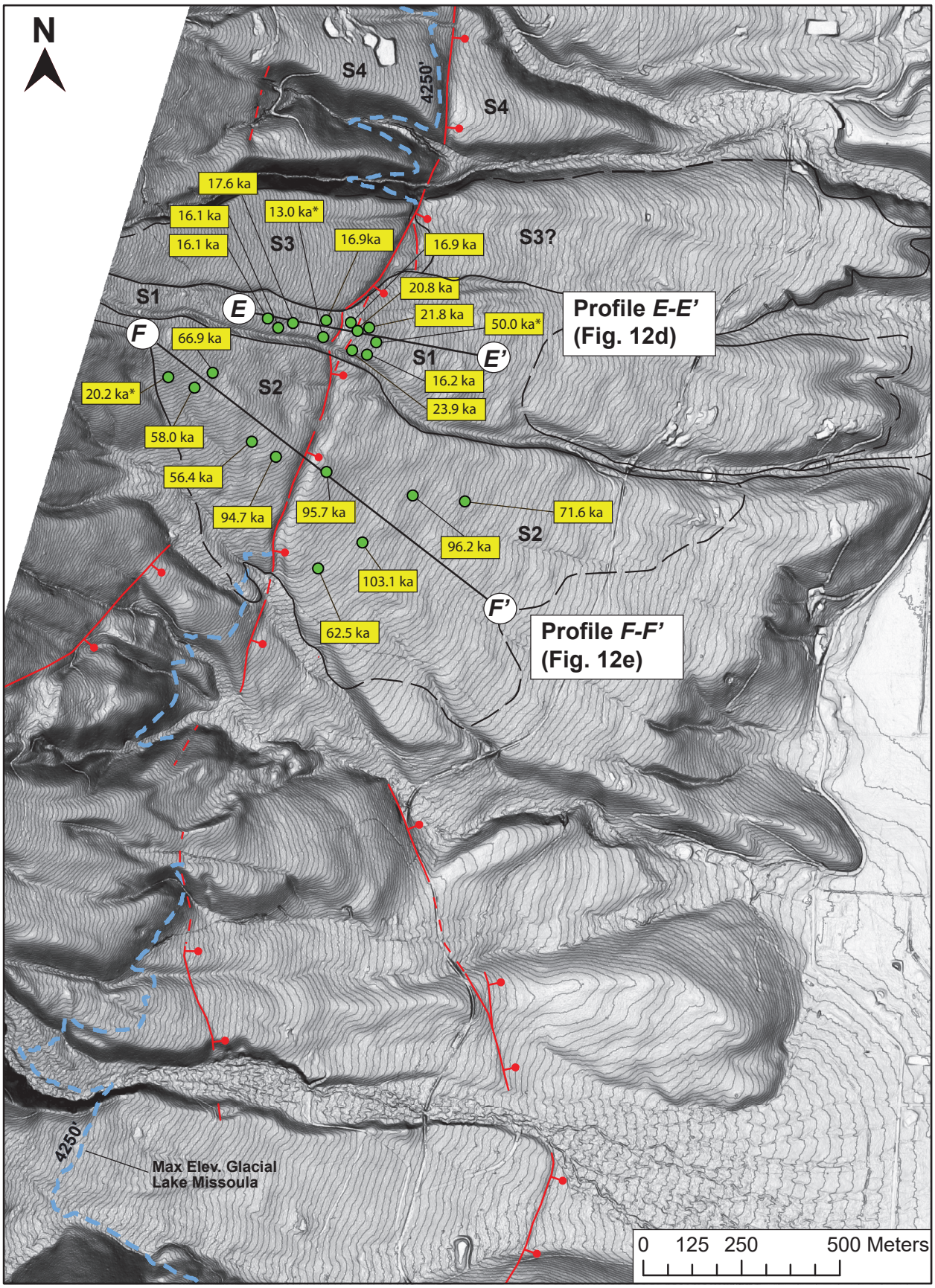

Figure 9. Detailed map of the Bitterroot fault scarps and surfaces S1–S4 at the Ward Creek fan showing cosmogenic ^{10}Be ages from sampled boulders. Base map is lidar slopeshade DEM with 2 m contour interval. See figure 4 for location and table 1 for age data results. S1, Pinedale young glacial debris fan (Qdfy); S2, middle-aged glacial debris fan (Qdfm); S3, middle-aged glacial debris fan (Qdfm) with bedrock pediment exposures; S4, Bedrock pediment surface with thin or no deposits preserved. *Ages interpreted as outliers based on probability density plots age models (figs. 10C, 10D).

Table 1. Cosmogenic ^{10}Be sample data and modeled surface exposure ages.

Sample	Lat	Long	Elv (m)	Sample Thickness (cm)[a]	Quartz Mass (g)[b]	Shield Correction[c]	^{10}Be/^{9}Be (x10^{-15})[d]	^{10}Be concentration (x10^{3} atoms/g SiO_2)[d]	Age (zero erosion; ka)[e,f]	Age (2 mm/ka erosion; ka)[e,f]
Lake Como moraine: **MC1 (Qgty)**										
LCS-Qgty-MC1-upper-1	46.057183	-114.236761	1,355	1	21.70	0.989542	291.0 ± 5.9	208.66 ± 4.49	15.2 ± 1.0	15.5 ± 1.0
LCS-Qgty-MC1-upper-2	46.057924	-114.234597	1,345	1	12.61	0.998349	156.5 ± 2.9	192.41 ± 3.86	14.0 ± 0.9	14.3 ± 0.9
LCS-Qgty-MC1-lower-3	46.058918	-114.232156	1,329	1	25.07	0.998845	343.7 ± 6.8	215.21 ± 4.55	15.8 ± 1.0	16.2 ± 1.0
LCS-Qgty-MC1-lower-4	46.05983	-114.23092	1,327	1	25.02	0.998562	335.2 ± 6.2	209.06 ± 4.19	15.4 ± 1.0	15.8 ± 1.0
LCS-Qgty-MC1-fault-5	46.058095	-114.234252	1,346	1	25.00	0.998455	326.1 ± 6.1	204.68 ± 4.10	14.9 ± 0.9	15.2 ± 1.0
Lake Como moraine: **MC2 (Qgty)**										
LCS-Qgty-MC2-lower-1	46.056855	-114.233578	1,366	1	24.99	0.997926	361.7 ± 7.7	225.40 ± 5.06	16.1 ± 1.0	16.5 ± 1.1
LCS-Qgty-MC2-lower-2	46.056771	-114.233924	1,367	1	9.86	0.998534	122.2 ± 2.3	191.78 ± 3.85	13.7 ± 0.9	14.1 ± 0.9
LCS-Qgty-MC2-lower-3	46.056698	-114.234311	1,373	1	24.99	0.996904	358.3 ± 6.2	224.21 ± 4.24	15.9 ± 1.0	16.3 ± 1.0
LCS-Qgty-MC2-upper-4	46.056456	-114.234938	1,380	1	25.10	0.998948	369.9 ± 7.1	231.45 ± 4.75	16.2 ± 1.0	16.6 ± 1.1
LCS-Qgty-MC2-upper-5	46.05633	-114.235173	1,387	1	25.03	0.998404	475.7 ± 9.1	297.54 ± 6.10	20.6 ± 1.3	21.2 ± 1.4
LCS-Qgty-MC2-upper-6	46.055926	-114.235900	1,395	1	25.01	0.997285	410.5 ± 6.7	254.25 ± 4.58	17.6 ± 1.1	18.1 ± 1.2
Ward Creek fan: **S1-Lower (Qdfy)**										
WCF-Qdfy-S1-lower-1	46.16152	-114.215608	1,321	1	19.98	0.996478	426.4 ± 7.7	331.02 ± 6.47	23.9 ± 1.5	24.8 ± 1.6
WCF-Qdfy-S1-lower-2	46.161483	-114.215093	1,315	1	20.01	0.996817	276.0 ± 5.2	219.44 ± 4.42	16.2 ± 1.0	16.6 ± 1.1
WCF-Qdfy-S1-lower-3	46.161692	-114.214868	1,315	1	20.03	0.996804	873.3 ± 10.8	691.31 ± 9.96	50.0 ± 3.1	54.9 ± 3.7
WCF-Qdfy-S1-lower-4	46.161944	-114.215443	1,323	1	20.01	0.959965	345.01 ± 5.4	274.34 ± 4.78	20.8 ± 1.3	21.4 ± 1.4
WCF-Qdfy-S1-lower-5	46.162041	-114.215004	1,317	1	20.02	0.99636	372.7 ± 6.0	297.06 ± 5.29	21.8 ± 1.4	22.5 ± 1.4
WCF-Qdfy-S1-lower-6	46.162061	-114.215653	1,325	1	20.01	0.996981	287.8 ± 5.4	229.40 ± 4.62	16.9 ± 1.1	17.4 ± 1.1
Ward Creek fan: **S1-Upper (Qdfy)**										
WCF-Qdfy-S1-upper-1	46.162111	-114.216519	1,335	1	20.09	0.99496	291.2 ± 5.5	229.49 ± 4.62	16.9 ± 1.1	17.3 ± 1.1
WCF-Qdfy-S1-upper-2	46.161994	-114.217598	1,348	1	20.00	0.996759	306.9 ± 5.7	245.26 ± 4.91	17.6 ± 1.1	18.1 ± 1.2
WCF-Qdfy-S1-upper-3	46.161917	-114.2182	1,355	1	20.24	0.995886	284.6 ± 6.5	224.17 ± 5.37	16.1 ± 1.0	16.5 ± 1.1
WCF-Qdfy-S1-upper-4	46.161944	-114.218611	1,360	1	20.02	0.996257	282.5 ± 5.7	225.06 ± 4.86	16.1 ± 1.0	16.5 ± 1.1
WCF-Qdfy-S1-upper-5	46.161755	-114.216547	1,334	1	20.01	0.99278	222.0 ± 4.1	176.26 ± 3.53	13.0 ± 0.8	13.3 ± 0.8
Ward Creek fan: **S2-Lower (Qdfm)**										
WCF-Qdfm-S2-lower-1	46.158698	-114.216225	1,310	1	25.00	0.996981	2395.2 ± 36.6	1307.93 ± 22.26	95.7 ± 6.0	113.8 ± 8.6
WCF-Qdfm-S2-lower-2	46.158274	-114.21334	1,280	1	25.00	0.996981	2066.4 ± 32.7	1282.49 ± 22.42	96.2 ± 6.0	114.4 ± 8.7
WCF-Qdfm-S2-lower-3	46.158213	-114.211642	1,267	1	25.02	0.996968	1517.1 ± 20.3	944.80 ± 14.49	71.6 ± 4.4	81.5 ± 5.8
WCF-Qdfm-S2-lower-4	46.156498	-114.216332	1,289	1	25.00	0.996969	1485.56 ± 18.05	836.78 ± 11.93	62.5 ± 3.9	69.5 ± 4.8
WCF-Qdfm-S2-lower-5	46.157164	-114.214925	1,285	1	25.04	0.996981	2221.6 ± 26.9	1381.75 ± 19.63	103.1 ± 6.4	124.7 ± 9.6
Ward Creek fan: **S2-Upper (Qdfm)**										
WCF-Qdfm-S2-upper-1	46.159341	-114.21877	1,344	1	25.02	0.996977	1264.9 ± 15.1	790.83 ± 11.12	56.4 ± 3.5	62 ± 4.2
WCF-Qdfm-S2-upper-2	46.160737	-114.220153	1,373	1	25.03	0.996758	1553.4 ± 26.5	966.22 ± 17.99	66.9 ± 4.2	75.4 ± 5.4
WCF-Qdfm-S2-upper-3	46.160691	-114.221614	1,384	1	25.00	0.996127	467.0 ± 7.9	291.70 ± 5.40	20.2 ± 1.3	20.9 ± 1.3
WCF-Qdfm-S2-upper-4	46.160441	-114.220668	1,374	1	25.01	0.996981	1336.3 ± 20.6	832.02 ± 14.23	58.0 ± 3.6	63.9 ± 4.4
WCF-Qdfm-S2-upper-5	46.159012	-114.217954	1,333	1	25.01	0.994069	2113.3 ± 24.9	1313.49 ± 18.32	94.7 ± 5.9	112.3 ± 8.5

[a]Sample thickness represents the total amount of material modeled for ^{10}Be exposure dating that includes 1.0 ± 0.5 cm of bedrock (granodiorite-gneiss) sampled interval.

[b]Average measured density of foliated biotite-muscovite granodiorite to gneiss boulder samples (2.57 ± 0.1 g/cm^3).

[c]Geometric shielding correction using CRONUS online calculator.

[d]All uncertainties reported at the 1σ. Blank corrected ^{10}Be/^{9}Be ratios. Total measurement uncertainty for the ^{10}Be concentration includes the uncertainty in the ^{9}Be carrier concentration, AMS measurement uncertainty, and uncertainty in the process blank correction. Combined, these uncertainties totaled to within 2% or 1σ.

[e]Ages reported using LSDn (nuclide-dependent scaling age models by Lifton-Stato-Dunai; Lifton and others, 2014).

[f]Assumed value of erosion rates for stable and resistant foliated granodiorite boulders that have preserved glacial erosional surfaces.

Note. Age results generated by CRONUS-Earth online calculators, Balco and others, 2008. https://hess.ess.washington.edu/, version 3

tively (table 1; appendix A). These two end-member scenarios in erosion rates are consistent for resistant granite-type bedrock lithology (Jackson and others, 1997; Duxbury and others, 2015; Margold and others, 2019). For completeness, full CRONUS outputs are shown in appendix A, and include calculations of age with 1σ uncertainties based on multiple production rate scaling schemes. However, for results presented in this work, we adopted the time-dependent scaling age model by Lifton–Stato–Dunai (LSD; Lifton and others, 2014). Modeled ages for each geomorphic surface combine multiple age results based on 5 to 11 boulders using the Probability Density Plotter of Vermeesch and others (2012), which integrates the range of erosion rate of e = 0 and e = 2 mm/ka, as minimum and maximum ages, respectively. A reported modeled age for each geomorphic surface is calculated by stacking and summing Gaussian bell curves of individual boulder ages with their respective uncertainties into a peak probability age distribution for a population of boulder ages. Detailed sample information, AMS results, and age model parameters for CRN ^{10}Be geochronology are provided in table 1 and appendix A.

Pinedale Glacial Moraine Ages—Lake Como

MC1(Qgty)

The youngest glacial till deposits sampled for CRN ^{10}Be dating were collected on surface boulders along a lateral moraine crest, referred to as MC1, in the Lake Como study site (figs. 7A, 7B, 8). The sampled surface MC1 represents the lowest and best-preserved moraine crest mapped south of Lake Como within the young glacial deposits (Qgty; fig. 4), sourced from the Pinedale-age Rock Creek Glacier. It extends nearly perpendicular to and across the Bitterroot fault (fig. 8). A total of five boulders were sampled along a 500-m length of the ENE–WSW-trending moraine crest, yielding ages from lowest to highest elevations (1327–1355 m) of 15.4 ± 1.0 ka, 15.8 ± 1.0 ka, 14.0 ± 0.9 ka, 14.9 ± 0.9 ka, and 15.2 ± 1.0 ka (fig. 8; table 1). Model age results and probability density plots combining all boulders from MC1 yield peak ages that range between 15.0 ± 0.4 ka and 15.4 ± 0.4 ka for erosion rates of e = 0 and e = 2 mm/ka, respectively (fig. 10A). The model age of ~15 ka for MC1 indicates no significant difference in the probability density plots between boulder ages with no erosion rate (15.0 ± 0.4 ka) and boulder ages that account for a 2 mm/ka erosion rate (15.4 ± 0.4). This sensitivity analysis suggests that potential erosion does not affect our age results.

MC2 (Qgty)

Another young glacial till deposit (Qgty) south of Lake Como was sampled on surface MC2, an ENE–WSW-trending lateral moraine crest that occupies a higher elevation than MC1 (figs. 7A, 8). A total of six boulders were sampled along a 250-m-long profile of MC2 offset by the Bitterroot fault scarp (fig. 8). The boulder sample population yields ages from lowest to highest elevation (1366–1395 m) of 16.1 ± 1.0 ka, 13.7 ± 0.9 ka, 15.9 ± 1.0 ka, 16.2 ± 1.0 ka, 20.6 ± 1.3 ka, and 17.6 ± 1.1 ka (fig. 8; table 1). Model age results of MC2 combining all boulders into probability density plots yield peak distribution ages that range between 16.4 ± 0.6 ka (e = 0) and 16.8 ± 0.6 ka (e = 2 mm/ka; fig. 10B). The model age of ~16–17 ka for MC2 indicates no significant age sensitivity between boulder ages that accounts for the range of erosion rates (e = 0 and e = 2 mm/ka).

Glacial Debris Fan Ages—Ward Creek Fan

S1 (Qdfy)

A young glacial debris fan deposit, referred as S1, was sampled for CRN ^{10}Be dating in the Ward Creek fan study site north of Lake Como (figs. 7C, 7D, 9). The sampled surface S1 represents the youngest mapped debris flows and fan surface (Qdfy; fig. 4) within the Ward Creek fan, sourced from the Pinedale-age Ward Cirque Glacier. Characteristics of the surface S1 that distinguish it as the youngest surface include well-preserved debris flow levees incised into older surfaces (S3–S4) and extensive boulder fields (figs. 7D, 9). S1 slopes to the east and is offset across the Bitterroot fault scarp with correlative hanging wall and footwall surfaces (figs. 7C, 9). Eleven boulders were sampled across a ~300-m-long profile. The six boulders sampled in the lower hanging wall fan surface (S1-Lower) yield ages of 23.9 ± 1.5 ka, 16.2 ± 1.0 ka, 50.0 ± 3.1 ka, 20.8 ± 1.3 ka, 21.8 ± 1.4 ka, and 16.9 ± 1.1 ka. (fig. 9; table 1). The five boulders sampled in the upper footwall surface (S1-Upper) yield ages of 16.9 ± 1.1 ka, 17.6 ± 1.1 ka, 16.1 ± 1.0 ka, 16.1 ± 1.0 ka, and 13.0 ± 0.8 ka (fig. 9; table 1). Model age results for S1 combing all boulders across both correlative surfaces yield peak ages that range between 16.6 ± 0.4 ka (e = 0) and 17.1 ± 0.5 ka (e = 2 mm/ka; fig. 10C). The model age of ~17 ka for S1 indicates no significant age sensitivity within the range of erosion rates. The ~50 ka boulder age result is interpreted as

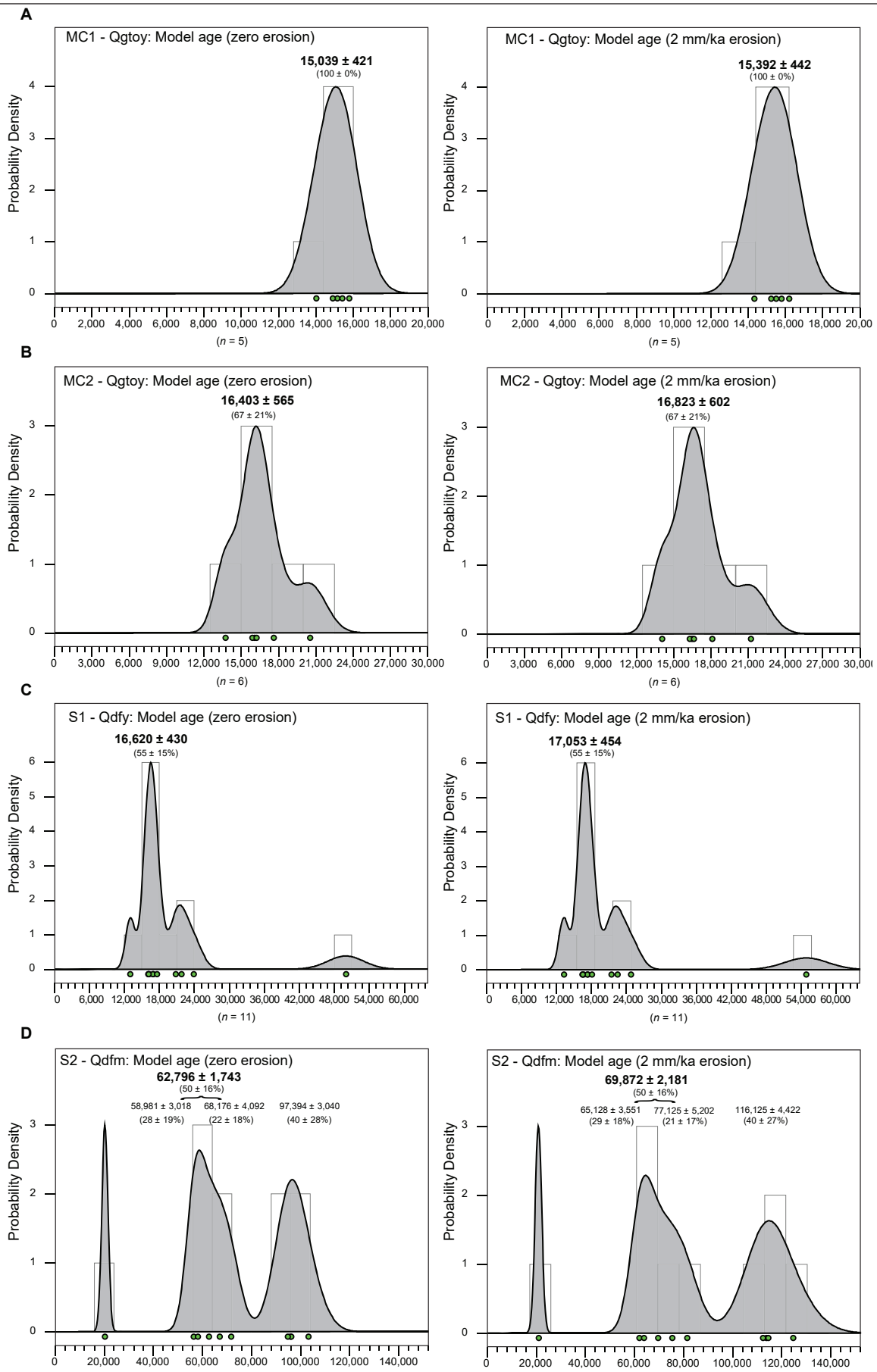

Figure 10. Probability density and histogram plots for each geomorphic unit with corresponding age model results in years for zero erosion (left) and 2 mm/ka erosion (right). (A, B) MC1–MC2 (Qgty), young Pinedale-age moraine crests in glacial till at Lake Como. (C) S1 (Qdfy), young Pinedale age glacial debris fan at Ward Creek Fan. (D) S2 (Qdfm), middle-aged glacial debris fan at Ward Creek fan.

an outlier, likely representing inheritance from older exposure history.

S2 (Qdfm)

Fan surface S2 is an older middle-aged glacial debris flow and fan deposit (Qdfm; fig. 4), mapped within the Ward Creek fan, that was sampled for CRN ^{10}Be dating (figs. 7E, 7F, 9). Surface S2 represents the largest east-sloping fan surface displaced by the Bitterroot fault. S2 is distinguished as a broad surface with sparse boulder fields incised by S1 and topographically lower than older surfaces S3–S4 (figs. 7E, 7F, 9). Ten boulders were collected along a ~750-m-long profile across both correlative lower hanging wall and upper footwall surfaces (figs. 7E, 9). Five boulders from the lower surface (S2-Lower) yield ages of 95.7 ± 6.0 ka, 96.2 ± 6.0 ka, 71.6 ± 4.4 ka, 62.5 ± 3.9 ka, and 103.1 ± 6.4 ka (fig. 9; table 1). Five boulders sampled in the upper surface (S2-Upper) yield ages 56.4 ± 3.5 ka, 66.9 ± 4.2 ka, 20.2 ± 1.3 ka, 58.0 ± 3.6 ka, and 94.7 ± 5.9 ka (fig. 9; table 1). Model age results for S2 across both correlative surfaces yield two main peak boulder age populations (excluding a single sample outlier of ~20 ka; fig. 10D). The youngest model peak age has a range between 62.8 ± 1.7 ka (e = 0) and 69.9 ± 2.2 ka (e = 2 mm/ka) that we interpret as the representative exposure age for S2 (fig. 10D). The older peak age (~97–116 ka; fig. 10D) is interpreted to represent either inheritance or an older sequence of debris flows that were not fully buried by thin boulder veneers of the younger debris flows (~63–70 ka). In addition, the topographic position of S2 coincides with mapped elevations of the Glacial Lake Missoula highstand shorelines (figs. 4, 9), which could have eroded and partly exposed older debris flow deposits at the surface. Values of erosion rates affect our model age for S2 by 10% between its minimum (~63 ka) and maximum (~70 ka), resulting in a larger degree of uncertainty for the modeled age on this surface.

Age Summary and Regional Correlation

Our CRN ^{10}Be age data provide an *in situ* chronology of surface exposure ages consistent with the mapped relations of Quaternary units. In the Lake Como area, CRN ^{10}Be age data from two sequences of the youngest and best-preserved Pinedale glacial moraines, MC1 and MC2, yield ages of ~15 ka and ~16–17 ka, respectively (figs. 8, 10A, 10B; table 1). Older mapped glacial moraines sourced from Rock Creek Glacier are consistent with our age results, indicating MC3 as likely early Pinedale in age (>20 ka), and MC4–MC6 as likely Bull Lake and older in age (>100 ka). In the Ward Creek fan area, age data from two glacial debris fans, S1 and S2, yield ages of ~17 ka and ~63–70 ka, respectively (figs. 9, 10C, 10D; table 1).

Our study sites in both Lake Como glacial moraines and debris fans sourced from the Ward Cirque Glacier (i.e., the Ward Creek fan) indicate similar Pinedale-age results between 15 and 17 ka, consistent with Pinedale ages reported in Greater Yellowstone and the Teton range (15–19 ka; Liccardi and Pierce; 2008). The glacial debris fan surface (S2) of ~63–70 ka at the Ward Creek fan may correlate to MIS 4 or Early Wisconsin Glaciation (~60–70 ka), while the older boulder age population in S2 of ~97–116 ka may represent inheritance exposure from MIS 6 or Bull Lake Glaciation (>100 ka; Pierce, 2004, and references therein; Liccardi and Pierce, 2008).

FAULT DISPLACEMENT RATES

The Bitterroot fault is evident through scarps on various geomorphic surfaces with vertical separation that ranges from 1 to 68 m and increases with age. Fault scarps truncate multiple sequences of sloping lateral moraine crests, glacial debris fans, and paleoshorelines that provide geomorphic strain markers to measure vertical separation using 1-m resolution lidar-based topographic profiles (figs. 8, 9, 11, 12). Measurements are based on vertical separations between footwall and hanging surfaces using linear regression topographic profiles that yielded best-matched correlative offset surfaces projected across the fault scarp (fig. 12). To determine deformation rates, we divided the amount of vertical separation and fault slip by our age data to derive vertical separation and fault slip rates, respectively (table 2). Fault dip and structural model constraints from map relations allow for the vertical component of deformation to be translated into fault slip rates. Fault slip rates are provided as a range with minimum and maximum values. All rates incorporate uncertainties in vertical separation based on the resolution of the selected linear regression topographic profiles and vertical accuracy of the lidar data (5 cm); range in calculated fault dips; and range of age results depending on analytical uncertainties and erosion rates (see table 2; appendix B).

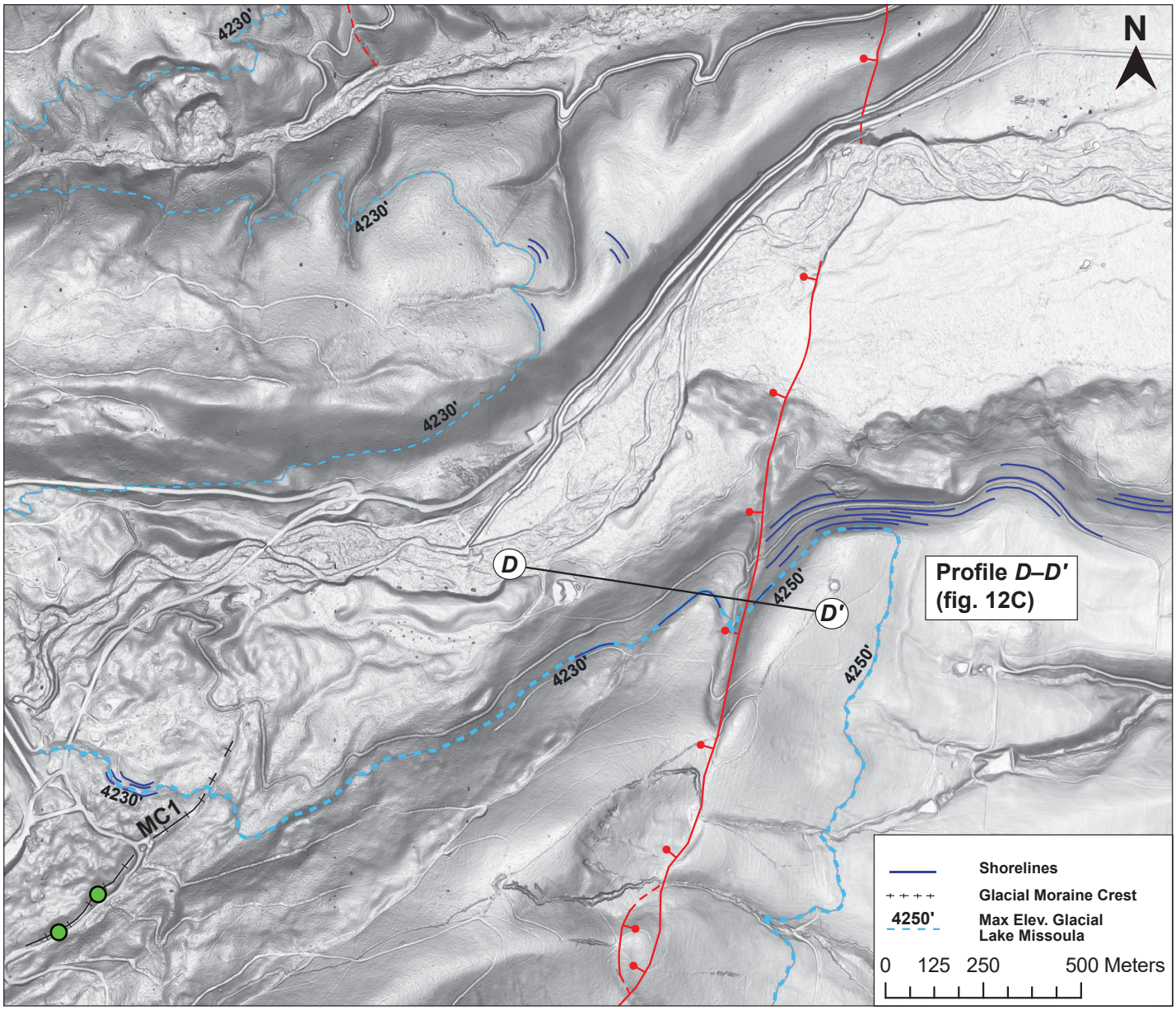

Figure 11. Detailed map of the Rock Creek study site showing antithetic fault strand of the Bitterroot fault and displaced Glacial Lake Missoula shorelines. Mapping of the maximum elevation shoreline indicates a vertical separation between the footwall (4,250 ft) and hanging wall (4,230 ft) correlative surfaces across the west-dipping fault (see profile D–D' in fig. 12C). The same shorelines are mapped inset into Lake Como moraine crest, MC1, dated at ~15 ka. Base map is lidar slopeshade DEM. See figure 3 for location. Age results are shown in table 1 and figure 10.

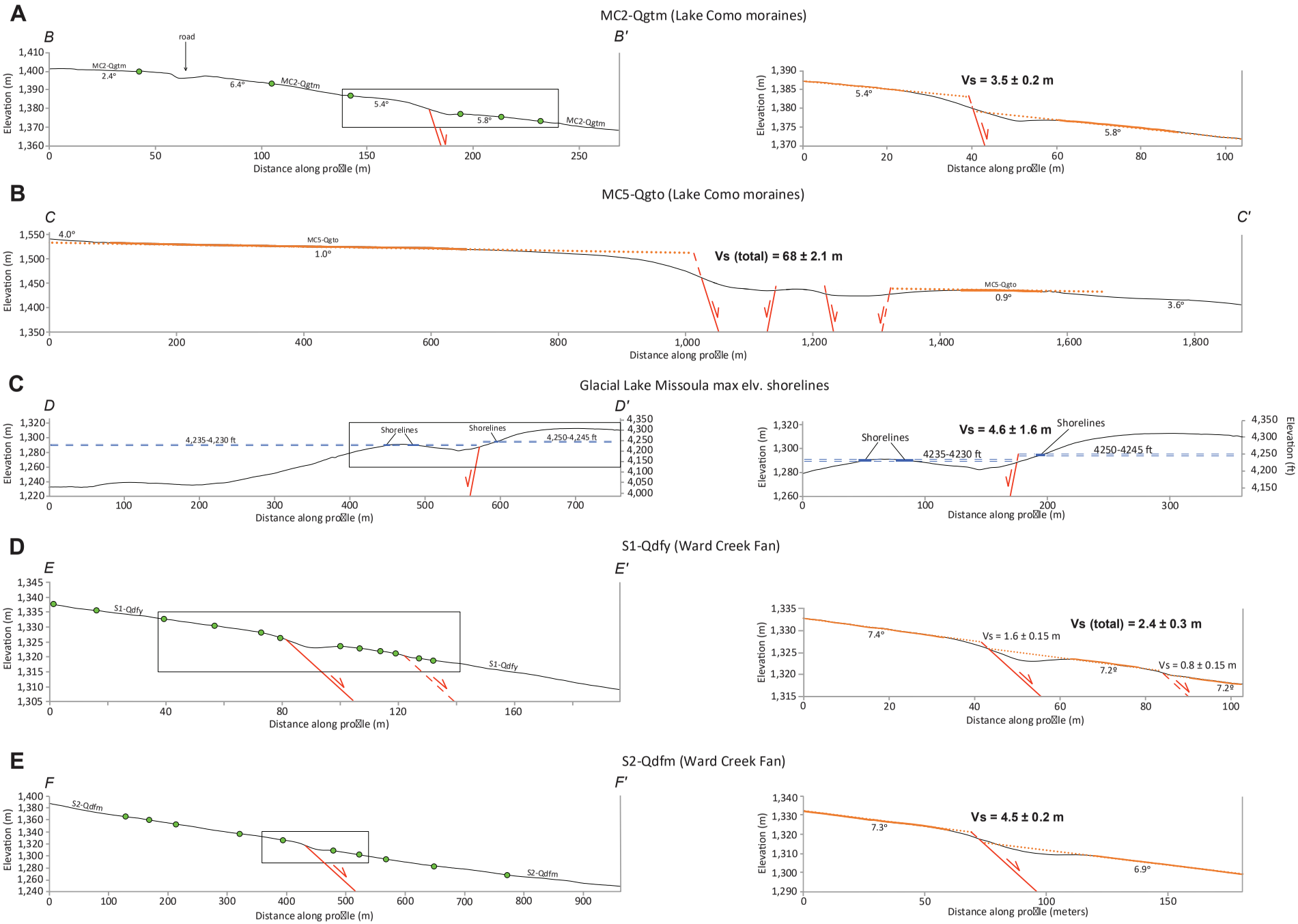

Figure 12. Vertical separation measurements (Vs) for multiple sites across the Bitterroot fault based on lidar-based regression slope topographic profiles of correlative hanging wall and footwall surfaces. (A) Surface MC2 (Qgty) at Lake Como; (B) Surface MC5 (Qgto) at Lake Como; (C) Glacial Lake Missoula highstand shorelines at Rock Creek; (D) Surface S1 (Qdfy) at Ward Creek fan; (E) Surface S2 (Qdfm) at Ward Creek fan. See figures 8, 9, and 11 for profile locations.

Table 2. Vertical separation and fault slip rates for the Bitterroot fault.

	Vertical Separation (m)	Min Surface Age (ka)	Max Surface Age (ka)	Fault Dip (deg.)	Vert. Separation Rate (mm/yr)	Fault Slip Rate (mm/yr)
Lake Como						
MC2—Pinedale moraine	3.5 ± 0.2	16.4 ± 0.6	16.8 ± 0.6	72 ± 6	0.19–0.23	0.20–0.25
Rock Creek						
Glacial Lake Missoula shorelines	4.6 ± 1.6	15.0 ± 0.4	15.4 ± 0.4	79 ± 9	0.19–0.42	0.19–0.45
Ward Creek fan						
S1—Pinedale debris fan	2.4 ± 0.3	16.6 ± 0.4	17.1 ± 0.5	48 ± 7	0.12–0.17	0.15–0.25
S2— Medium-aged debris fan	4.5 ± 0.2	62.8 ± 1.7	69.9 ± 2.2	48 ± 7	0.06–0.08	0.07–0.12

Note. Measured values of vertical separation, range in calculated fault dip (see appendix 2), and range of surface ages for offset marker units. Using these parameters, we calculated vertical separation rates and fault slip rates with corresponding uncertainties, which are based on the maximum and minimum possible values in the rate calculation.

Lake Como

Pinedale Glacial Moraines: MC1–MC2 (Qgty)

South of Lake Como, the trace of the Bitterroot fault cuts young Pinedale-age glacial till deposits (Qgty) and its lateral moraines MC1–MC2 (fig. 8). Mapping and lidar data do not indicate any clear fault scarps across the moraine crest MC1 (fig. 8). A well-exposed N–S-trending east-dipping fault scarp lineament and ENE–WSW-sloping MC2 provide a well-preserved geomorphic strain marker of vertical separation (figs. 8, 12A). Topographic profile measurements yield a vertical separation of 3.5 ± 0.2 m for correlative offset surfaces across the fault scarp (fig. 12A; profile B–B′). Fault dip calculations using 3-point problem measurements along the main trace of the Bitterroot fault south of Lake Como indicate the fault dips range between 66 and 78° to the east (figs. 5, 8; appendix B). Rate calculations using an age range of 16.4 ± 0.6 ka to 16.8 ± 0.6 ka for MC2 yield a vertical separation rate of 0.19–0.23 mm/yr and fault slip rate of 0.20–0.25 mm/yr (table 2).

Bull Lake Glacial Moraines: MC4–MC6 (Qgto)

The trace of the Bitterroot fault displaces older glacial till deposits (Qgto) with three mapped moraine crests (MC4–MC6) interpreted as Bull Lake age or older (fig. 8). Mapping and field observations based on smooth geomorphic surfaces, inflated soil horizons with limited exposed boulder fields, and elevations are consistent with presumed Bull Lake or older surface ages. A selected topographic profile measurement along MC5 with a maximum fault scarp height of ~75 m (fig. 6A) yields a long-wavelength vertical separation of 68 ± 2.1 m for correlative lower and upper surfaces displaced across multiple strands of the Bitterroot fault (fig. 12B; profile C–C′). No *in situ* age data yet exist for MC5 or any other Bull Lake glacial till in Western Montana. However, boulders exposed in the glacially sourced debris fan surface S2 at the Ward Creek fan provide evidence of Bull Lake age results in the southern Bitterroot (fig. 9). If we assume MC5 is Bull Lake in age (~140–150 ka; Liccardi and Pierce, 2018), a vertical separation of 68 ± 2.1 m displaced on the 66–78° fault would yield an estimated vertical separation rate of ~0.4–0.5 mm/yr and slip rate of ~0.5–0.6 mm/yr.

Rock Creek

Glacial Lake Missoula Shorelines

Paleoshorelines provide another set of geomorphic strain marker to measure vertical separation across fault scarps produced during the Quaternary activity along the Bitterroot fault. Mapping using lidar-based slopemap index analyses identified multiple stair-step sequences of wave-cut shorelines associated with Glacial Lake Missoula in the Bitterroot Valley (figs. 4, 11, 13). Maximum elevations on shorelines that range in elevation between 4,250 ft and 4,230 ft along the Bitterroot Valley correlate with the Glacial Lake Missoula

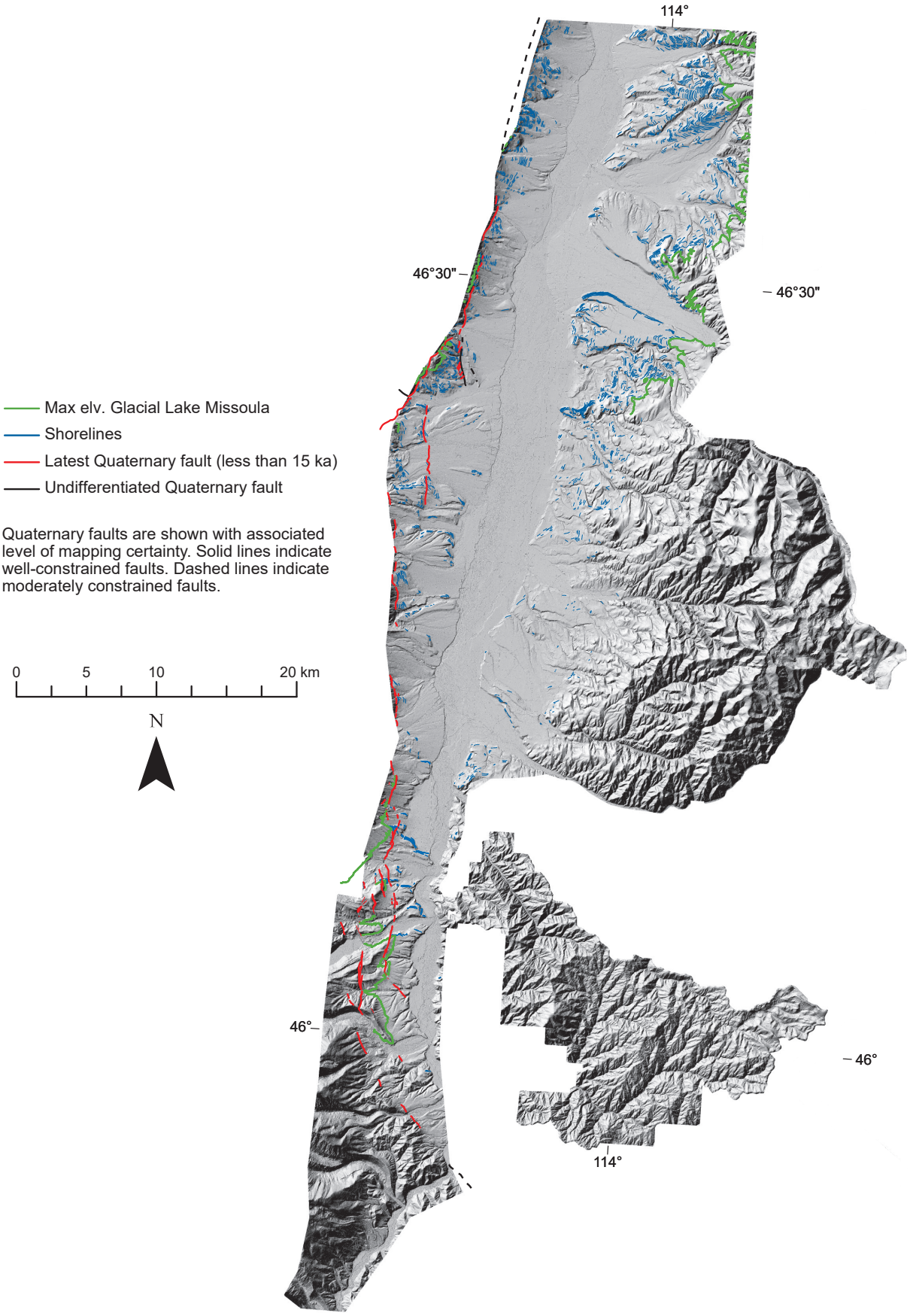

Figure 13. Compilation of mapped shorelines (blue) and Quaternary fault scarps (red) in the Bitterroot Valley using available lidar data, showing the maximum elevation shorelines of Glacial Lake Missoula (green) that ranges between 4,250 ft and 4,230 ft. Note many shorelines demonstrate vertical separation across the Bitterroot fault. Location of lidar coverage shown in figure 2.

highstand that flooded the Bitterroot and Missoula Valleys in the latest Pleistocene (figs. 11, 13; Smith and others, 2018). In the Rock Creek study site, east of Lake Como, these maximum elevation shorelines are displaced across a west-facing fault scarp interpreted as an antithetic strand of the Bitterroot fault (fig. 11). Measurements of displacement rates on this antithetic fault provide constraints on subsurface kinematic link and slip distribution with the main strand of the Bitterroot fault, which potentially rupture simultaneously during earthquakes.

Topographic profile measurements yield vertical separation of 4.6 ± 1.6 m for correlative shorelines across the footwall (4,250 ft) and hanging wall (4,230 ft) of the west-dipping fault, with the uncertainty based on the map correlation of maximum elevation shorelines (fig. 12C, profile D–D′). Fault dips of 70–88° to the east are based on fault dip calculations using 3-point problem measurements along the mapped trace of the antithetic fault (figs. 5, 11; appendix B). These maximum elevation shorelines of Glacial Lake Missoula are mapped near Lake Como Dam and inset into the youngest dated Pinedale glacial moraine deposits of S1-Qgty (~15.0 ka; figs. 8, 11). Our age results of ~15 ka represent a maximum age for the timing of Glacial Lake Missoula highstand shoreline formation. This age is broadly consistent with estimates of the youngest dated Glacial Lake Missoula sediments associated with a deep lake filling sequence that occurred prior to 13.4–13.7 ka before drainage (Smith and others, 2018). Rate calculations using an age range of 15.0 ± 0.4 ka and 15.4 ± 0.4 ka yield a vertical separation rate of 0.19–0.42 mm/yr and fault slip rate of 0.19–0.45 mm/yr (table 2).

Ward Creek Fan

Young Pinedale-Age Glacial Debris Fan: S1 (Qdfy)

In the Ward Creek study site, north of Lake Como, the Bitterroot fault offsets young Pinedale-age glacial debris fan deposits S1 (Qdfy; fig. 9). The main fault trace mapped across the Ward Creek fan is an NNE–SSW-trending east-facing fault scarp that offsets an east-sloping debris fan surface S1 (figs. 7C, 9). A mapped secondary east-facing fault scarp is inferred to offset S1 as a local hanging wall fault splay to the Bitterroot fault (figs. 9, 12D). Topographic profile measurements yield a total vertical separation of 2.4 ± 0.3 m for correlative surfaces S1 offset across both the main fault scarp and its fault splay (fig. 12D, profile E–E′). Fault dip calculations using 3-point measurements constrain the fault geometry near the Ward Creek fan area, indicating the main trace of the fault dips 41–55° to the east (figs. 5, 9; appendix B). We assume the dip of the secondary fault strand is similar to that of the main fault trace. Rate calculations using an age range of 16.6 ± 0.4 ka and 17.1 ± 0.5 ka for S1 yield a vertical separation rate of 0.12–0.17 mm/yr and fault slip rate of 0.15–0.25 mm/yr (table 2).

Middle-Aged Glacial Debris Fan: S2 (Qdfm)

The Bitterroot fault displaces older glacial debris fan deposit S2 (Qdfm) within the Ward Creek fan (figs. 7E, 9). S2 is the largest debris fan surface, extending >500 m across the hanging wall and footwall of the Bitterroot fault scarp. The main trace of the Bitterroot fault across surface S2 consists of a well-exposed and continuous east-facing scarp with no significant fault splays. Topographic profile measurements yield a vertical separation of 4.5 ± 0.1 m for correlative S2 surfaces (fig. 12E, profile F–F′). The fault dips 41–55°E to the east, based on 3-point problem methods (figs. 5, 9; appendix B). Rate calculations using an age range of 62.8 ± 1.7 ka to 69.9 ± 2.2 ka for S2 yield a vertical separation rate of 0.06–0.08 mm/yr and fault slip rate of 0.07–0.12 mm/yr (table 2). Exposure model ages and resulting slip rate calculations for S2 include a larger degree of uncertainty compared to the slip rates for other sites. We attribute this greater uncertainty to the apparent complex depositional history of multiple debris flow sequences, inheritance, and/or post-surface modification.

Slip Rate Summary for the Bitterroot Fault

Projected on-plane fault slip rates on the Bitterroot fault range between 0.1 mm/yr and 0.3 mm/yr associated with the main fault strand of the Bitterroot fault (fig. 14; table 2). At Lake Como, vertical separation of a young Pinedale moraine (MC2; figs. 8, 12A) yields a slip rate of 0.2–0.3 mm/yr. At the Ward Creek fan, vertically separated glacial debris fans (S1–S2; figs. 9, 12D, 12E) yield slip rates that range between 0.2–0.3 mm/yr (S1) and 0.1 mm/yr (S2). Our results indicate possible higher slip rates near Lake Como (0.2–0.3 mm/yr) compared to the Ward Creek fan (0.1–0.3 mm/yr) further north (fig. 14). However, the rates broadly overlap between the two study sites, with a total along-strike range of 0.1–0.3 mm/yr for the southern

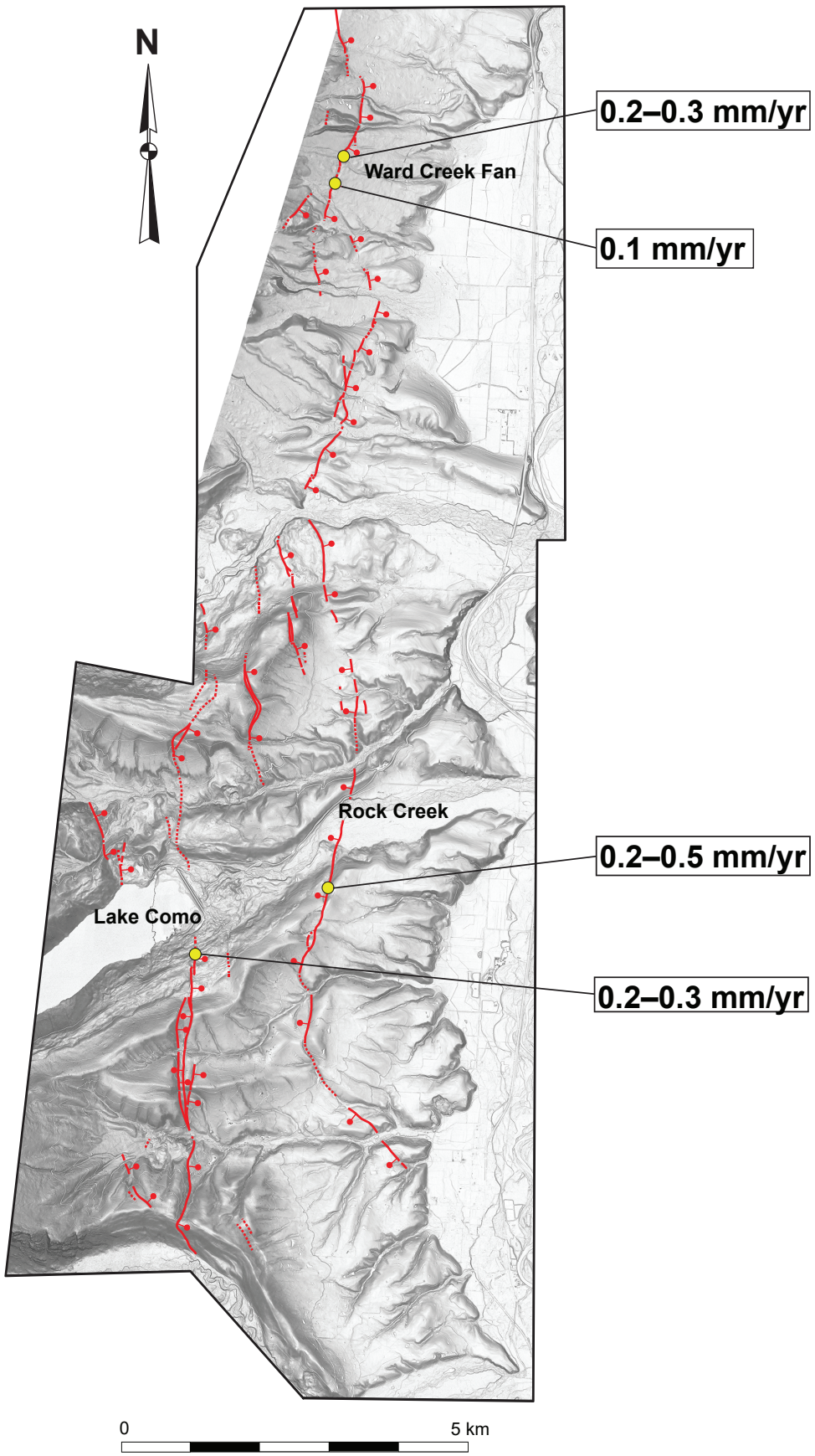

Figure 14. Slip rates distribution map along the southern Bitterroot fault showing results from our study sites (yellow). Rates on the main east-dipping fault strand range between 0.1 and 0.3 mm/yr (table 2). Slip rates on the antithetic west-dipping fault are 0.2–0.5 mm/yr, which broadly overlap with the rates on the main strand of 0.2–0.3 mm/yr for the Lake Como area.

section of the Bitterroot fault (fig. 14). Our lowest slip rate site on S2 (0.1mm/yr) in the Ward Creek fan (figs. 9, 14) may underestimate slip rates for the Bitterroot fault because of the larger degree of uncertainty in the age results due to inferred complex exposure history and/or post-surface modification (fig. 10D).

Slip rates on the antithetic fault strand of the Bitterroot fault are 0.2–0.5 mm/yr, based on displaced Glacial Lake Missoula highstand shorelines at the Rock Creek study site (figs. 11, 14). Roughly equal slip rates partitioned on both the main fault strand near Lake Como (0.2–0.3 mm/yr) and antithetic fault strand (0.2–0.5 mm/yr) of the Bitterroot fault are consistent with our structural framework interpretation (fig. 5). Total slip and net extension accommodated on the hanging wall block (east of the antithetic fault) cannot exceed the total budget of 0.2–0.3 mm/yr accommodated across the main fault strand. Fault block kinematics based on our slip rate results dictate two possible fault models:

1. local differential deformation near the antithetic fault (e.g., east-directed hanging wall rotation) due to slip vectors as a high-angle fault (fig. 5A); or

2. uniform fault-bounded block displacement (e.g., downdropping of a local graben) due to lateral slip vectors at depth as a low-angle fault (fig. 5B).

Either fault model yields permissible solutions and fault block kinematics that can be tested with further detailed mapping of Bitterroot fault hanging wall strata along the Bitterroot Valley.

IMPLICATIONS FOR EARTHQUAKE POTENTIAL

New understanding of the displacement history along the Bitterroot fault provides constraints on the potential earthquake hazards to the Bitterroot and Missoula Valleys (figs. 1, 2).

Our fault mapping and results of geological slip rates suggest the Bitterroot fault is likely the primary seismogenic fault system within the Missoula and Bitterroot Valleys capable of releasing interseismic strain accumulation via surface-rupturing earthquakes. Fault geometries frame the size of the potential earthquake. The length of the Bitterroot fault extends more than ~100 km (103–105 km) along the mountain front (fig. 2). Empirical scaling relationships indicate that a fault length of this dimension could generate a maximum of ~Mw 7.2 during full-length normal-fault rupturing earthquakes (Wells and Coppersmith, 1994; Stirling and others, 2013; https://earthquake.usgs.gov/scenarios/catalog/mt2016/; USGS, 2016). An earthquake scenario of M7.2 (based on ~100-km-long surface rupture along the Bitterroot fault) is forecasted to produce "heavy" earthquake damage with 0.75 g peak ground acceleration, 86 cm/sec peak velocity, and Modified Mercalli Intensity IX shaking (https://earthquake.usgs.gov/scenarios/catalog/mt2016/).

Lack of significant recorded microseismicity during the past 40 yr within the Bitterroot Valley (fig. 1B; Stickney, 2015, 2022) may suggest the Bitterroot fault is locked at depth. We speculate the Bitterroot fault is likely characterized by a millennia-timescale earthquake recurrence interval based on a loading slip rate of <1 mm/yr and the absence of historical earthquakes.

An earthquake and associated ground shaking on the Bitterroot fault could profoundly affect the Bitterroot Valley and nearby Missoula metropolitan area, including critical infrastructure such as dams, canals, pipelines, transportation corridors, and power lines. Unfortunately, earthquake history and recurrence interval are unknown for this fault, although the seismic risk is potentially high given the length of the fault, evidence of late Quaternary fault scarps, and proximity of the rapidly growing population in the Missoula and Bitterroot Valleys. Paleoseismic data are therefore needed to improve seismic source characterization of the Bitterroot fault and to improve the related hazard assessment. This study has identified multiple paleoseismic trench sites on the Bitterroot fault near Lake Como and Ward Creek study sites with the goal of developing a Holocene paleoearthquake chronology. In addition, improved constraints of the deeper Bitterroot fault geometry are needed to address the possibility of a low-angle seismogenic fault. An earthquake scenario on a low-angle fault would suggest a larger seismogenic width and seismic hazard with an earthquake Mw >7.2.

CONCLUSION

Our results provide the first *in situ* age data and slip rates for seismic source characterization of the Bitterroot fault. Lidar-based mapping indicates multiple late Quaternary fault scarps with vertical offset in glacial deposits. The ^{10}Be cosmogenic radionuclides surface exposure dating technique and vertical separation measurements constrain slip rates at four sites along the southern Bitterroot fault.

Near Como Dam, we dated two Pinedale-age glacial moraines to ~15 ka and ~16–17 ka. On the main strand of the Bitterroot fault, an offset ~16–17 ka glacial moraine yields a fault slip rate of 0.2–0.3 mm/yr. Glacial Lake Missoula shorelines, which are offset across an antithetic strand of the Bitterroot fault, and are inset into a dated ~15 ka glacial moraine, yield a fault slip rate of 0.2–0.5 mm/yr. In the Ward Creek fan located north of Lake Como, we dated two glacial debris fans to ~17 ka and ~63–70 ka. Vertical separations and age constraints across the Bitterroot fault yield fault slip rates of 0.1–0.3 mm/yr on the ~17 ka debris fan surface and 0.1 mm/yr on the ~63–70 ka debris fan surface. Our results indicate broadly consistent fault slip rates for the main fault segments at Lake Como (0.2–0.3 mm/yr) and the Ward Creek fan (0.1–0.3 mm/yr) with an along-strike total range of 0.1–0.3 mm/yr for the southern Bitterroot fault.

Subsurface fault models provide two permissible structural solutions for the Bitterroot fault. Steep normal faults at the surface and in the shallow subsurface either could remain high angle or merge at depth into a low-angle fault model geometry. Our mapping and cross-sections indicate both of these fault models are viable, with major implications for the seismogenic fault width and earthquake potential of the Bitterroot fault.

This study builds on the previous work by Stickney and Lonn (2018) to reevaluate existing regional seismic source models for western Montana. Our findings reinforce the need to include the Bitterroot fault in the NSHM as a seismogenic source that could profoundly impact the Bitterroot and Missoula Valleys, producing an up to ~100-km-long fault rupture during an earthquake along the Bitterroot Valley.

ACKNOWLEDGMENTS

This material is based upon work supported by the U.S. Geological Survey under Grant G20AP00047 and received financial support from the Montana Bureau of Mines and Geology. Thoughtful and constructive reviews from Alexandra Hatem, Sylvia Nicovich, and Petr Yakovlev helped clarify and improve this manuscript. We are thankful for lab assistance from Connie Thompson and Kristina Okonski; GIS support from Yiwen Li, Paul Thale, and Iris Smith; and editorial assistance from Madeline Gotkowitz, Susan Smith, and Susan Barth at the MBMG. We also are thankful for many fruitful discussions and insights on the project results with Ryan Gold, Chris DuRoss, and Alexandra Hatem from the USGS, and Ralph Klinger, Sylvia Nicovich, and Colin Chupik from the U.S. Bureau of Reclamation. Prepared in part by LLNL under Contract DE-AC52-07NA27344.

REFERENCES

Arabasz, W.J., and Smith, R.B., 1981, Earthquake prediction in the Intermountain seismic belt—An intraplate extensional regime, *in* Simpson, D.W., and Richards, P.G., eds., Earthquake prediction: An international review, v. 1: American Geophysical Union, Washington, D.C., p. 248–258, doi: 10.1029/ME004p0248.

Balco, G., Stone, J.O., Lifton, N.A., and Dunai, T.J., 2008, A complete and easily accessible means of calculating surface exposure ages or erosion rates from ^{10}Be and ^{26}Al measurements: Quaternary Geochronology, v. 3, p. 174–195.

Berg, R.B., and Lonn, J.D., 1996, Preliminary geologic map of the Nez Perce Pass 30 x 60 minute quadrangle, Montana: Montana Bureau of Mines and Geology Open-File Report 339, scale 1:100,000.

Ditchburn, R.G., and Whitehead N.E., 1994, The separation of ^{10}Be from silicates: 3d Workshop of the South Pacific Environmental Radioactivity Association, 4–7.

Duxbury, J., Bierman, P.R., Portenga, E.W., Pavich, M.J., Southworth, S., and Freeman, S.P., 2015, Erosion rates in and around Shenandoah National Park, Virginia, determined using analysis of cosmogenic ^{10}Be: American Journal of Science, v. 315, p. 46–76.

Foster, D.A., and Raza, A., 2002, Low-temperature thermochronological record of exhumation of the Bitterroot metamorphic core complex, northern Cordilleran Orogen: Tectonophysics, v. 349, no. 1–4, p. 23–36.

Foster, D.A., Schaferb, C., Fanning, C.M., and Hyndman, D.W., 2001, Relationships between crustal partial melting, plutonism, orogeny, and exhumation: Idaho–Bitterroot batholith: Tectonophysics, v. 342, p. 313–350.

Frankel, K.F., Brantley, K.S., Dolan, J.F., Finkel, R.C., Klinger, R.E., Knott, J.R., Machette, M.N., Owen, L.A., Phillips, F.M., Slate, J.L., and Wernicke, B.P., 2007, Cosmogenic ^{10}Be and ^{36}Cl geochronology of offset alluvial fans along the northern Death Valley fault zone: Implications for transient strain in the eastern California shear zone: Journal of Geophysical Research, v. 112, p. B06407, doi: 10.1029/2006JB004350.

Gosse, J.C., and Phillips, F.M., 2001, Terrestrial in situ cosmogenic nuclides: Theory and application: Quaternary Science Reviews, v. 20, p. 1475–1560.

Hatem, A.E., Collett, C.M., Gold, R.D., Briggs, R.W., Angster, S.A., Field, E.H., Anderson, M., Ben Horin, J.Y., Dawson, T., DeLong, S., DuRoss, C., Thompson Jobe, J., Kleber, E., Knudsen, K.L., Koehler, R., Koning, D., Lifton, Z., Madin, I., Mauch, J., Morgan, M., Pearthree, P., Petersen, M., Pollitz, F., Scharer, K., Powers, P., Sherrod, B., Stickney, M., Wittke, S., and Zachariasen, J., 2022, Earthquake geology inputs for the National Seismic Hazard Model (NSHM) 2023, v. 2.0: U.S. Geological Survey data release, doi: https://doi.org/10.5066/P9AU713N.

Hidy, A.J., Brown, T.A., Tumey, S.J., Zimmerman, S.R., Gharibyan, N., Frank, M., and Bench, G., 2018, A new ^{7}Be AMS capability established at CAMS and the potential for large datasets: Nuclear Instruments and Methods in Physics Research Section B: Beam Interactions with Materials and Atoms, v. 414, p. 126–132.

Hyndman, D.W., 1980, Bitterroot dome–Sapphire tectonic block, an example of a plutonic core–gneiss–dome complex with its detached suprastructure, *in* Crittenden, M.D., Coney, P.J., and Davis, G.H., eds., Cordilleran Metamorphic Core Complexes: Geological Society of America Memoir, v. 153, p. 427–443.

Jackson, L.E., Phillips, F.M., Shimamura, K., and Little, E.C., 1997, Cosmogenic ^{36}Cl dating of the Foothills erratics train, Alberta, Canada: Geology, v. 25, p. 195–198.

Kohl, C.P., and Nishiizumi, K., 1992, Chemical isolation of quartz for measurement of in situ–produced cosmogenic nuclides: Geochimica et Cosmochimica Acta, v. 56, p. 3583–3587, doi: 10.1016/0016-7037(92)90401-4.

Konizeski, R.L., 1958, Pliocene vertebrate fauna from the Bitterroot Valley, Montana, and its stratigraphic significance: Geological Society of America Bulletin, v. 69, p. 325–345.

Lal, D., 1991, Cosmic ray labeling of erosion surfaces in situ nuclide production rates and erosion models: Earth Planetary Science Letters, v. 104, p. 424–439.

Licciardi, J., 2000, Alpine glacier and pluvial lake records of Late Pleistocene climate variability in the western United States: Corvallis, Ore., Oregon State University, Ph.D. dissertation, 155 p.

Licciardi, J.M., and Pierce, K.L., 2008, Cosmogenic exposure-age chronologies of Pinedale and Bull Lake glaciations in greater Yellowstone and the Teton Range, USA: Quaternary Science Reviews, v. 27, no. 7–8, p. 814–831.

Licciardi, J.M., and Pierce, K.L., 2018, History and dynamics of the Greater Yellowstone Glacial System during the last two glaciations: Quaternary Science Reviews, v. 200, p. 1–33, ISSN 0277-3791, doi: doi.org/10.1016/j.quascirev.2018.08.027.

Lifton, N., Sato, T., and Dunai, T.J., 2014, Scaling in situ cosmogenic nuclide production rates using analytical approximations to atmospheric cosmic-ray fluxes: Earth and Planetary Science Letters, v. 386, p. 149–160.

Lonn, J.D., and Berg, R.B., 1996, Preliminary geologic map of the Hamilton 30 x 60 minute quadrangle, Montana: Montana Bureau of Mines and Geology Open-File Report 340, scale 1:100,000.

Lonn, J.D., and Gavillot, Y., 2022, Geologic map of the southern Bitterroot fault, Bitterroot Valley, western Montana: Montana Bureau of Mines

and Geology Geologic Map 83, 1 sheet, scale 1:24,000.

Lonn, J.D., and Sears, J.W., 2001, Geology of the Bitterroot Valley, shaded relief: Montana Bureau of Mines and Geology Open-File Report 441-C, 1 sheet, scale 1:48,000.

Lonn, J.D., Burmester, R.F., Lewis, R.S., and McFaddan, M.D., 2020, The Mesoproterozoic Belt Supergroup, *in* Metesh, J.J., and Vuke, S.M., eds., Geology of Montana—Geologic History: Montana Bureau of Mines and Geology Special Publication 122, v. 1, 38 p., available at https://mbmg.mtech.edu/pdf/geologyvolume/Lonn_Belt-Final.pdf.

Margold, M., Gosse, J., Hidy, A., Woywitka, R., Young, J., and Froese, D., 2019, Beryllium-10 dating of the Foothills Erratics Train in Alberta, Canada, indicates detachment of the Laurentide Ice Sheet from the Rocky Mountains at ~15 ka: Quaternary Research, v. 92, p. 1–14, doi: 10.1017/qua.2019.10.

Mason, D.B., 1996, Earthquake magnitude potential of the Intermountain Seismic Belt, USA, from surface-parameter scaling of late quaternary faults: Bulletin of the Seismological Society of America, v. 86, no. 5, p. 1487–1506.

McMurtrey, R.G., Konizeski R.L., Johnson, M.V., and Bartells, J.H., 1972, Geology and water resources of the Bitterroot Valley, southwestern Montana: U.S. Geological Survey Water Supply Paper 1889, 80 p., scale 1:125,000.

Myers, W.B., and Hamilton, W., 1964, Deformation accompanying the Hebgen Lake earthquake of August 17, 1959, The Hebgen Lake, Montana, Earthquake of August 17, 1959 (v. 435, p. 55–98): Geological Survey Professional Paper: Washington, D.C., U.S. Government Printing Office.

Norbeck, P.M., 1980, Preliminary evaluation of deep aquifers in the Bitterroot and Missoula valleys in western Montana: Montana Bureau of Mines and Geology Open-File Report 46, 15 p.

Petersen M.D., Shumway A.M., Powers P.M., and others, 2020, The 2018 update of the US National Seismic Hazard Model: Overview of model and implications. Earthquake Spectra, v. 36, no. 1, p.5–41, doi:10.1177/8755293019878199.

Pierce, K.L., 2004, Pleistocene glaciations of the Rocky Mountains: Developments in Quaternary Sciences: Amsterdam, Elsevier, v. 1, p. 63–76.

Sbar, M.L., Barazangi, M., Dorman, J., Scholz, C.H., and Smith, R.B., 1972, Tectonics of the intermountain seismic belt, western United States: Micro earthquake seismicity and the composite fault place solutions: Geological Society of America Bulletin, v. 83, no. 1, p. 13–28, doi: 10.1130/0016-7606(1972)83[13:TOTISB]2.0.CO;2.

Smith, L., 2006, Altitude of the bedrock surface in the Bitterroot Valley: Missoula and Ravalli Counties, Montana: Montana Bureau of Mines and Geology Montana Ground-Water Assessment Atlas 4, Part B, Map 5, 1 sheet, scale 1:125,000.

Smith, L., Sohbati, R., Buylaert, J-P., Lian, O.B., Murray, A., and Jain, M., 2018, Timing of lake-level changes for a deep last-glacial Lake Missoula: Optical dating of the Garden Gulch area, Montana, USA: Quaternary Science Reviews, v. 183, p. 23–35.

Smith, R.B., and Arabasz, W.J., 1991, Seismicity of the intermountain seismic belt, *in* Slemmons, D.B., Engdahl, E.R., Zoback, M.D., and Blackwell, D.D., eds., Neotectonics of North America: Geological Society of America, p. 185–228, doi: 10.1130/DNAG-CSMS-NEO.185.

Stickney, M.C., 2015, Seismicity within and adjacent to the eastern Lewis and Clark line, west-central Montana: Northwest Geology v. 44, p. 19–36.

Stickney, M.C., 2022, Earthquakes and seismographic monitoring in Montana, *in* Metesh, J.J., and Gammons, C.H., eds., Geology of Montana—Special Topics: Montana Bureau of Mines and Geology Special Publication 122, v. 2, 50 p.

Stickney, M.C., and Lonn, J.D., 2018, Investigation of late Quaternary Fault scarps along the Bitterroot Fault in western Montana: Montana Bureau of Mines and Geology Report of Investigation 24, 16 p., 2 plates.

Stirling, M., Goded, T., Berryman, K., and Litchfield, N., 2013, Selection of earthquake scaling relationships for seismic-hazard analysis: Bulletin of the Seismological Society of America, v. 103, no. 6, p. 2993–3011, doi: 10.1785/0120130052.

Stone, J.O., 2000, Air pressure and cosmogenic isotope production: Journal of Geophysical Research, v. 105, p. 23753–23759, doi:10.1029/2000JB900181.

U.S. Geological Survey, 2016, Montana Earthquake Scenario Catalog, available at https://earthquake.usgs.gov/scenarios/catalog/mt2016/ [Accessed October 27, 2021].

APPENDIX A:

MODEL PARAMETERS AND DATA INPUT

Appendix A. Model parameters and data input for modeling cosmogenic nuclide ^{10}Be surface exposure dating using CRONUS Age Calculator.

CRONUS Age Calculator—Data input

Batch ID	Sample	Lat	Long	Elv (m)	Elv/Pressure handling flag	Sample thickness (cm)[a]	Sample density (g/cm3)[b]	Shield Correction[c]	Erosion rates (cm/yr)[d]	Date sample collection	Isotope	Mineral	Be10 Conc.	Error	Standard
	Ward Creek Fan:														
	S1-Lower (Qdfy)														
54	WCF-Qdfy-S1-lower-1	46.16152	-114.215608	1321	std	1	2.57	0.996478	0 / 0.0002	2020	Be-10	quartz	330078.2768	6407.248159	KNSTD
54	WCF-Qdfy-S1-lower-2	46.161483	-114.215093	1315	std	1	2.57	0.996817	0 / 0.0002	2020	Be-10	quartz	218492.1546	4375.701757	KNSTD
54	WCF-Qdfy-S1-lower-3	46.161692	-114.214868	1315	std	1	2.57	0.996804	0 / 0.0002	2020	Be-10	quartz	690483.573	9991.253068	KNSTD
54	WCF-Qdfy-S1-lower-4	46.161944	-114.215443	1323	std	1	2.57	0.959965	0 / 0.0002	2020	Be-10	quartz	274901.061	4958.767371	KNSTD
54	WCF-Qdfy-S1-lower-5	46.162041	-114.215004	1317	std	1	2.57	0.99636	0 / 0.0002	2020	Be-10	quartz	298276.2115	5328.345806	KNSTD
54	WCF-Qdfy-S1-lower-6	46.162061	-114.215653	1325	std	1	2.57	0.996981	0 / 0.0002	2020	Be-10	quartz	230636.0593	4664.240646	KNSTD
	Ward Creek Fan:														
	S1-Upper (Qdfy)														
54	WCF-Qdfy-S1-upper-1	46.162111	-114.216519	1335	std	1	2.57	0.99496	0 / 0.0002	2020	Be-10	quartz	230898.4748	4642.023484	KNSTD
54	WCF-Qdfy-S1-upper-2	46.161994	-114.217598	1348	std	1	2.57	0.996759	0 / 0.0002	2020	Be-10	quartz	244452.327	4892.820977	KNSTD
54	WCF-Qdfy-S1-upper-3	46.161917	-114.2182	1355	std	1	2.57	0.995886	0 / 0.0002	2020	Be-10	quartz	223523.3538	5289.774374	KNSTD
54	WCF-Qdfy-S1-upper-4	46.161944	-114.218611	1360	std	1	2.57	0.996257	0 / 0.0002	2020	Be-10	quartz	224820.1801	4539.623279	KNSTD
54	WCF-Qdfy-S1-upper-5	46.161755	-114.216547	1334	std	1	2.57	0.99278	0 / 0.0002	2020	Be-10	quartz	176165.3906	3532.384624	KNSTD
	Ward Creek Fan:														
	S2-Lower (Qdfm)														
58	WCF-Qdfm-S2-lower-1	46.158698	-114.216225	1310	std	1	2.57	0.996981	0 / 0.0002	2020	Be-10	quartz	1310826.191	20218.82544	KNSTD
58	WCF-Qdfm-S2-lower-2	46.158274	-114.21334	1280	std	1	2.57	0.996981	0 / 0.0002	2020	Be-10	quartz	1285181.112	19901.07275	KNSTD
58	WCF-Qdfm-S2-lower-3	46.158213	-114.211642	1267	std	1	2.57	0.996968	0 / 0.0002	2020	Be-10	quartz	947747.846	14295.30561	KNSTD
58	WCF-Qdfm-S2-lower-4	46.156498	-114.216332	1289	std	1	2.57	0.996969	0 / 0.0002	2020	Be-10	quartz	840718.4401	11886.1754	KNSTD
58	WCF-Qdfm-S2-lower-5	46.157164	-114.214925	1285	std	1	2.57	0.996981	0 / 0.0002	2020	Be-10	quartz	1385910.482	19536.94888	KNSTD
	Ward Creek Fan:														
	S2-Upper (Qdfm)														
58	WCF-Qdfm-S2-upper-1	46.159341	-114.21877	1344	std	1	2.57	0.996977	0 / 0.0002	2020	Be-10	quartz	790824.1104	11124.11507	KNSTD
58	WCF-Qdfm-S2-upper-2	46.160737	-114.220153	1373	std	1	2.57	0.996758	0 / 0.0002	2020	Be-10	quartz	966217.3548	17989.24779	KNSTD
58	WCF-Qdfm-S2-upper-3	46.160691	-114.221614	1384	std	1	2.57	0.996127	0 / 0.0002	2020	Be-10	quartz	291694.2867	5395.249434	KNSTD
58	WCF-Qdfm-S2-upper-4	46.160441	-114.220668	1374	std	1	2.57	0.996981	0 / 0.0002	2020	Be-10	quartz	833961.7162	14034.16989	KNSTD
58	WCF-Qdfm-S2-upper-5	46.159012	-114.217954	1333	std	1	2.57	0.994069	0 / 0.0002	2020	Be-10	quartz	1317388.847	20320.41003	KNSTD
	Lake Como Morraine:														
	MC1 (Qgty)														
57	LCS-Qgty-MC1-upper-1	46.057183	-114.236761	1355	std	1	2.57	0.989542	0 / 0.0002	2020	Be-10	quartz	208360.0312	4319.992433	KNSTD
57	LCS-Qgty-MC1-upper-2	46.057924	-114.234597	1345	std	1	2.57	0.998349	0 / 0.0002	2020	Be-10	quartz	192048.2846	3852.790069	KNSTD
57	LCS-Qgty-MC1-lower-3	46.058918	-114.232156	1329	std	1	2.57	0.998845	0 / 0.0002	2020	Be-10	quartz	215010.7245	4402.807248	KNSTD
57	LCS-Qgty-MC1-lower-4	46.05983	-114.23092	1327	std	1	2.57	0.998562	0 / 0.0002	2020	Be-10	quartz	209373.6448	4196.588083	KNSTD
57	LCS-Qgty-MC1-fault-5	46.058095	-114.234252	1346	std	1	2.57	0.998455	0 / 0.0002	2020	Be-10	quartz	204992.5209	4105.170905	KNSTD
	Lake Como Morraine:														
	MC2 (Qgty)														
57	LCS-Qgty-MC2-lower-1	46.056855	-114.233578	1366	std	1	2.57	0.997926	0 / 0.0002	2020	Be-10	quartz	225658.4867	5031.415896	KNSTD
57	LCS-Qgty-MC2-lower-2	46.056771	-114.233924	1367	std	1	2.57	0.998534	0 / 0.0002	2020	Be-10	quartz	191997.9871	3864.2781	KNSTD
57	LCS-Qgty-MC2-lower-3	46.056698	-114.234311	1373	std	1	2.57	0.996904	0 / 0.0002	2020	Be-10	quartz	224065.9626	4340.248394	KNSTD
57	LCS-Qgty-MC2-upper-4	46.056456	-114.234938	1380	std	1	2.57	0.998948	0 / 0.0002	2020	Be-10	quartz	230696.5105	4694.30873	KNSTD
57	LCS-Qgty-MC2-upper-5	46.05633	-114.235173	1387	std	1	2.57	0.998404	0 / 0.0002	2020	Be-10	quartz	297086.3593	6066.126402	KNSTD
57	LCS-Qgty-MC2-upper-6	46.055926	-114.235900	1395	std	1	2.57	0.997285	0 / 0.0002	2020	Be-10	quartz	254071.8333	4574.686848	KNSTD

[a]Sample thickness represents the total amount of material modeled for 10Be exposure dating that includes 1 ± 0.5 cm of bedrock (granodiorite-gneiss) sampled interval.
[b]Average measured density of boulder foliated biotite-muscovite granodiorite to gneiss samples (2.57 ± 0.1 g/cm3).
[c]Geometric shielding correction using CRONUS online calculator.
[d]Assumed value of erosion rates for stabe and resistant foliated granodiorite boulders that have preserved glacial erosional surfaces.

Topographic Shielding Measurements

Sample	Strike of surface (azimuth°)	Dip of surface (°)	Azimuth (0-360°)	Inclination (0-90°)	Shield Correction
Ward Creek Fan:					
S1-Lower (Qdfy)					
WCF-Qdfy-S1-lower-1	281	10	0,45,90,135,170,210,230,270,335	2,2,2,3,3,5,9,18,10	0.996478
WCF-Qdfy-S1-lower-2	248	7	0,45,90,135,170,210,230,270,335	2,2,2,3,3,5,9,18,10	0.996817
WCF-Qdfy-S1-lower-3	328	10	0,45,90,135,170,210,230,270,335	2,2,2,3,3,5,9,18,10	0.996804
WCF-Qdfy-S1-lower-4	355	36	0,45,90,135,170,210,230,270,335	2,2,2,3,3,5,9,18,10	0.959965
WCF-Qdfy-S1-lower-5	139	10	0,45,90,135,170,210,230,270,335	2,2,2,3,3,5,9,18,10	0.99636
WCF-Qdfy-S1-lower-6	212	0	0,45,90,135,170,210,230,270,335	2,2,2,3,3,5,9,18,10	0.996981
Ward Creek Fan:					
S1-Upper (Qdfy)					
WCF-Qdfy-S1-upper-1	316	16	0,45,90,135,170,210,230,270,335	2,2,2,3,3,5,9,18,10	0.99496
WCF-Qdfy-S1-upper-2	350	13	0,45,90,135,170,210,230,270,335	2,2,2,3,3,5,9,18,10	0.996759
WCF-Qdfy-S1-upper-3	35	16	0,45,90,135,170,210,230,270,335	2,2,2,3,3,5,9,18,10	0.995886
WCF-Qdfy-S1-upper-4	11	17	0,45,90,135,170,210,230,270,335	2,2,2,3,3,5,9,18,10	0.996257
WCF-Qdfy-S1-upper-5	15	21	0,45,90,135,170,210,230,270,335	2,2,2,3,3,5,9,18,10	0.99278
Ward Creek Fan:					
S2-Lower (Qdfm)					
WCF-Qdfm-S2-lower-1	12	4	0,45,90,135,170,210,230,270,335	2,2,2,3,3,5,9,18,10	0.996981
WCF-Qdfm-S2-lower-2	24	2	0,45,90,135,170,210,230,270,335	2,2,2,3,3,5,9,18,10	0.996981
WCF-Qdfm-S2-lower-3	297	5	0,45,90,135,170,210,230,270,335	2,2,2,3,3,5,9,18,10	0.996968
WCF-Qdfm-S2-lower-4	49	6	0,45,90,135,170,210,230,270,335	2,2,2,3,3,5,9,18,10	0.996969
WCF-Qdfm-S2-lower-5	9	4	0,45,90,135,170,210,230,270,335	2,2,2,3,3,5,9,18,10	0.996981
Ward Creek Fan:					
S2-Upper (Qdfm)					
WCF-Qdfm-S2-upper-1	205	3	0,45,90,135,170,210,230,270,335	2,2,2,3,3,5,9,18,10	0.996977
WCF-Qdfm-S2-upper-2	34	13	0,45,90,135,170,210,230,270,335	2,2,2,3,3,5,9,18,10	0.996758
WCF-Qdfm-S2-upper-3	140	11	0,45,90,135,170,210,230,270,335	2,2,2,3,3,5,9,18,10	0.996127
WCF-Qdfm-S2-upper-4	66	2	0,45,90,135,170,210,230,270,335	2,2,2,3,3,5,9,18,10	0.996981
WCF-Qdfm-S2-upper-5	128	16	0,45,90,135,170,210,230,270,335	2,2,2,3,3,5,9,18,10	0.994069
Lake Como Morraine:					
MC1 (Qgty)					
LCS-Qgty-MC1-upper-1	68	21	0,45,80,110,130,160,210,240,250,265,280,340	3,3,2,4,11,18,12,10,11,0,10,7	0.989542
LCS-Qgty-MC1-upper-2	322	10	0,45,75,110,160,200,250,260,280,340	1,1,3,8,10,11,8,0,10,6	0.998349
LCS-Qgty-MC1-lower-3	191	9	0,45,90,135,180,230,265,280,340	3,1,5,8,10,6,0,8,7	0.998845
LCS-Qgty-MC1-lower-4	271	1	0,45,90,135,180,220,230,250,260,280,340	2,2,6,10,10,10,10,6,0,9,7	0.998562
LCS-Qgty-MC1-fault-5	341	8	0,45,75,110,160,200,250,260,280,340	1,1,3,8,10,11,8,0,10,6	0.998455
Lake Como Morraine:					
MC2 (Qgty)					
LCS-Qgty-MC2-lower-1	45	11	0,30,130,185,250,290,330	0,2,4,9,13,7,7	0.997926
LCS-Qgty-MC2-lower-2	113	9	0,30,120,180,250,290,340	0,1,4,9,9,9,7	0.998534
LCS-Qgty-MC2-lower-3	328	16	0,30,65,130,170,205,250,300,340	2,1,1,3,8,13,10,6,5	0.996904
LCS-Qgty-MC2-upper-4	3	0	0,30,50,90,130,190,240,280,340	4,0,2,4,5,8,10,9,7	0.998948
LCS-Qgty-MC2-upper-5	18	12	0,45,65,95,130,180,240,255,285,340	0,0,3,4,5,9,8,10,6,7	0.998404
LCS-Qgty-MC2-upper-6	201	14	0,45,90,135,180,225,265,280,340	0,0,4,6,8,10,0,10,8	0.997285

CRONUS Age Calculator—Age model results for zero erosion rate

Sample	Nuclide	St			Lm			LSDn		
		Age (yr)	Internal error	External error (yr)	Age (yr)	Internal error (yr)	External error (yr)	Age (yr)	Internal error	External error
Ward Creek Fan:										
S1-Lower (Qdfy)										
WCF-Qdfy-S1-lower-1	Be-10 (qtz)	24633	481	2016	23718	463	1848	23868	466	1491
WCF-Qdfy-S1-lower-2	Be-10 (qtz)	16342	329	1337	16011	322	1248	16209	326	1014
WCF-Qdfy-S1-lower-3	Be-10 (qtz)	52106	764	4240	49773	729	3849	49962	732	3073
WCF-Qdfy-S1-lower-4	Be-10 (qtz)	21236	385	1730	20592	373	1597	20764	377	1288
WCF-Qdfy-S1-lower-5	Be-10 (qtz)	22318	401	1818	21583	388	1673	21747	391	1348
WCF-Qdfy-S1-lower-6	Be-10 (qtz)	17118	348	1402	16746	340	1306	16935	344	1061
Ward Creek Fan:										
S1-Upper (Qdfy)										
WCF-Qdfy-S1-upper-1	Be-10 (qtz)	17039	344	1395	16670	337	1300	16853	340	1055
WCF-Qdfy-S1-upper-2	Be-10 (qtz)	17831	358	1460	17417	350	1358	17584	353	1100
WCF-Qdfy-S1-upper-3	Be-10 (qtz)	16225	386	1343	15899	378	1255	16069	382	1026
WCF-Qdfy-S1-upper-4	Be-10 (qtz)	16250	329	1330	15923	323	1242	16091	326	1007
WCF-Qdfy-S1-upper-5	Be-10 (qtz)	13026	262	1065	12803	258	997	12990	261	812
Ward Creek Fan:										
S2-Lower (Qdfm)										
WCF-Qdfm-S2-lower-1	Be-10 (qtz)	100490	1590	8295	95522	1509	7492	95728	1512	5980
WCF-Qdfm-S2-lower-2	Be-10 (qtz)	100851	1602	8327	95870	1521	7521	96187	1526	6011
WCF-Qdfm-S2-lower-3	Be-10 (qtz)	74641	1147	6116	71261	1094	5550	71635	1100	4441
WCF-Qdfm-S2-lower-4	Be-10 (qtz)	64936	933	5297	62201	893	4822	62535	898	3854
WCF-Qdfm-S2-lower-5	Be-10 (qtz)	108543	1572	8951	102901	1489	8058	103133	1492	6420
Ward Creek Fan:										
S2-Upper (Qdfm)										
WCF-Qdfm-S2-upper-1	Be-10 (qtz)	58442	834	4759	56112	800	4342	56349	804	3466
WCF-Qdfm-S2-upper-2	Be-10 (qtz)	70045	1327	5786	66836	1265	5252	66888	1266	4208
WCF-Qdfm-S2-upper-3	Be-10 (qtz)	20726	385	1690	20118	374	1562	20244	376	1258
WCF-Qdfm-S2-upper-4	Be-10 (qtz)	60251	1029	4941	57839	988	4511	58002	990	3611
WCF-Qdfm-S2-upper-5	Be-10 (qtz)	99478	1573	8209	94585	1494	7416	94712	1496	5915
Lake Como Morraine:										
MC1 (Qgty)										
LCS-Qgty-MC1-upper-1	Be-10 (qtz)	15245	317	1250	14975	312	1170	15146	315	951
LCS-Qgty-MC1-upper-2	Be-10 (qtz)	14031	282	1148	13811	278	1076	14017	282	877
LCS-Qgty-MC1-lower-3	Be-10 (qtz)	15903	327	1303	15590	320	1217	15782	324	990
LCS-Qgty-MC1-lower-4	Be-10 (qtz)	15513	312	1269	15222	306	1186	15414	310	964
LCS-Qgty-MC1-fault-5	Be-10 (qtz)	14968	301	1224	14720	296	1147	14900	300	932
Lake Como Morraine:										
MC2 (Qgty)										
LCS-Qgty-MC2-lower-1	Be-10 (qtz)	16239	364	1338	15910	356	1250	16082	360	1018
LCS-Qgty-MC2-lower-2	Be-10 (qtz)	13789	278	1128	13570	274	1057	13740	277	859
LCS-Qgty-MC2-lower-3	Be-10 (qtz)	16054	312	1311	15733	306	1224	15897	309	991
LCS-Qgty-MC2-upper-4	Be-10 (qtz)	16409	335	1344	16074	328	1254	16233	332	1017
LCS-Qgty-MC2-upper-5	Be-10 (qtz)	21053	432	1727	20417	419	1595	20547	422	1289
LCS-Qgty-MC2-upper-6	Be-10 (qtz)	17901	324	1457	17479	316	1354	17621	319	1092

St: Time-independent scaling age model by Stone et al. (2000), which is based on Lal (1991).
Lm: Time-dependent scaling age model by Lal/Stone that accounts for geomagnetic field variations.
LSDn: Nuclide-dependent scaling age model by Lifton-Stato-Dunai.

Age results generated by CRONUS-Earth online calculators, Balco et al. (2008).
https://hess.ess.washington.edu/
version 3

CRONUS Age Calculator—Age model results for 2 mm/ka erosion rate

Sample	Nuclide	St			Lm			LSDn		
		Age (yr)	Internal error	External error (yr)	Age (yr)	Internal error (yr)	External error (yr)	Age (yr)	Internal error	External error
Ward Creek Fan:										
S1-Lower (Qdfy)										
WCF-Qdfy-S1-lower-1	Be-10 (qtz)	25659	523	2190	24641	501	1999	24796	504	1613
WCF-Qdfy-S1-lower-2	Be-10 (qtz)	16784	347	1411	16421	339	1314	16618	343	1068
WCF-Qdfy-S1-lower-3	Be-10 (qtz)	57035	919	5102	54543	875	4618	54875	881	3697
WCF-Qdfy-S1-lower-4	Be-10 (qtz)	21993	413	1857	21271	399	1707	21443	403	1377
WCF-Qdfy-S1-lower-5	Be-10 (qtz)	23155	432	1958	22331	416	1795	22497	419	1446
WCF-Qdfy-S1-lower-6	Be-10 (qtz)	17604	368	1484	17196	359	1379	17385	363	1120
Ward Creek Fan:										
S1-Upper (Qdfy)										
WCF-Qdfy-S1-upper-1	Be-10 (qtz)	17521	364	1476	17119	355	1372	17301	359	1114
WCF-Qdfy-S1-upper-2	Be-10 (qtz)	18360	380	1548	17904	371	1437	18076	374	1165
WCF-Qdfy-S1-upper-3	Be-10 (qtz)	16661	407	1417	16307	398	1322	16474	402	1080
WCF-Qdfy-S1-upper-4	Be-10 (qtz)	16688	348	1404	16332	340	1308	16495	343	1061
WCF-Qdfy-S1-upper-5	Be-10 (qtz)	13305	273	1112	13086	269	1041	13264	273	847
Ward Creek Fan:										
S2-Lower (Qdfm)										
WCF-Qdfm-S2-lower-1	Be-10 (qtz)	121632	2371	12375	113691	2182	10830	113768	2184	8633
WCF-Qdfm-S2-lower-2	Be-10 (qtz)	122165	2394	12444	114198	2202	10891	114433	2208	8697
WCF-Qdfm-S2-lower-3	Be-10 (qtz)	85411	1516	8083	81004	1425	7230	81487	1435	5795
WCF-Qdfo-S2-lower-4	Be-10 (qtz)	72864	1183	6715	69205	1116	6022	69549	1122	4814
WCF-Qdfm-S2-lower-5	Be-10 (qtz)	133867	2444	13915	124580	2233	12087	124693	2235	9619
Ward Creek Fan:										
S2-Upper (Qdfm)										
WCF-Qdfm-S2-upper-1	Be-10 (qtz)	64751	1030	5873	61754	976	5296	61983	980	4227
WCF-Qdfm-S2-upper-2	Be-10 (qtz)	79410	1719	7496	75356	1619	6719	75441	1621	5386
WCF-Qdfm-S2-upper-3	Be-10 (qtz)	21445	413	1811	20768	399	1668	20892	402	1343
WCF-Qdfm-S2-upper-4	Be-10 (qtz)	66991	1280	6143	63762	1211	5530	63874	1213	4422
WCF-Qdfm-S2-upper-5	Be-10 (qtz)	120130	2335	12185	112331	2150	10672	112296	2149	8496
Lake Como Morraine:										
MC1 (Qgty)										
LCS-Qgty-MC1-upper-1	Be-10 (qtz)	15629	334	1314	15325	327	1227	15504	331	998
LCS-Qgty-MC1-upper-2	Be-10 (qtz)	14356	296	1202	14131	291	1126	14323	295	917
LCS-Qgty-MC1-lower-3	Be-10 (qtz)	16322	345	1373	15982	337	1280	16185	342	1042
LCS-Qgty-MC1-lower-4	Be-10 (qtz)	15911	329	1336	15591	322	1246	15789	326	1013
LCS-Qgty-MC1-fault-5	Be-10 (qtz)	15338	316	1286	15054	310	1202	15236	314	977
Lake Como Morraine:										
MC2 (Qgty)										
LCS-Qgty-MC2-lower-1	Be-10 (qtz)	16676	384	1412	16318	375	1316	16486	379	1072
LCS-Qgty-MC2-lower-2	Be-10 (qtz)	14103	291	1180	13882	287	1106	14069	291	900
LCS-Qgty-MC2-lower-3	Be-10 (qtz)	16481	329	1382	16137	322	1288	16301	326	1044
LCS-Qgty-MC2-upper-4	Be-10 (qtz)	16855	354	1419	16484	346	1321	16646	349	1072
LCS-Qgty-MC2-upper-5	Be-10 (qtz)	21797	464	1852	21084	448	1705	21212	451	1378
LCS-Qgty-MC2-upper-6	Be-10 (qtz)	18435	344	1546	17970	335	1433	18116	337	1156

St: Time-independent scaling age model by Stone et al. (2000), which is based on Lal (1991).
Lm: Time-dependent scaling age model by Lal/Stone that accounts for geomagnetic field variations.
LSDn: Nuclide-dependent scaling age model by Lifton-Stato-Dunai.

Age results generated by CRONUS-Earth online calculators, Blaco et al. (2008).
https://hess.ess.washington.edu/
version 3

APPENDIX B:

FAULT DIP CALCULATIONS

Appendix B. Results, explanation, and site descriptions for fault dip calculations on the Bitterroot fault using 3-point problem methods.

	Tringulated map distance^{x} (m)	Unc. (m)	Upper fault trace elev. ^{Hb}(m)	Unc. (m)	Lower fault trace elev. ^{Ha}(m)	Unc. (m)	Elev. Difference (m)	Unc. (m)	Calculated fault dip av. (°)	Calculated fault dip Max (°)	48
Lake Como area											
Station 1 (*Como ridge* s)	8.8	2.1	1418.0	1.0	1391.0	1.0	27.0	2.0	**72**	**77**	**66**
Station 2 (*Como ridge* s)	14.9	2.1	1449.0	1.0	1391.0	1.0	58.0	2.0	**76**	**78**	**73**
Station 3 (*Bunkhouse Creek*)*	112.1	2.1	1385.0	1.0	1329.0	1.0	56.0	2.0	27	28	25
Station 4 (*Bunkhouse Creek*)*	129.1	2.1	1403.7^{interpolated}	1.0	1329.0	1.0	74.7	2.0	30	31	29
Ward Creed Fan area											
Station 5 (*Ward Creek*)	15.0	2.1	1287.0	1.0	1270.5	0.5	16.5	1.5	**48**	**54**	**41**
Station 6 (*Ward Creek*)	17.1	2.1	1290.2^{interpolated}	1.0	1270.5	0.5	19.7	1.5	**49**	**55**	**43**
Rock Creek area											
Station 7 (*Rock Creek*)	22.0	2.1	1279.5^{interpolated}	0.5	1210.5	0.5	27.0	1.0	**72**	**74**	**70**
Station 8 (*Rock Creek*)	4.9	2.1	1287.8^{interpolated}	0.5	1215	0.2	72.8	1.0	**86**	**88**	**84**

** Stations where fault dip calculations using 3-point problem methods failed to meet criteria of consistent mapped fault trace strike direction (step in fault trace) and were not included for the total range of fault dip values and fault slip rate calculations for the Lake Como sites (MC2; Table 2).*

Fault dip calculations using 3-point problem (Method 1): Equivalent fault trace elevation across topography.

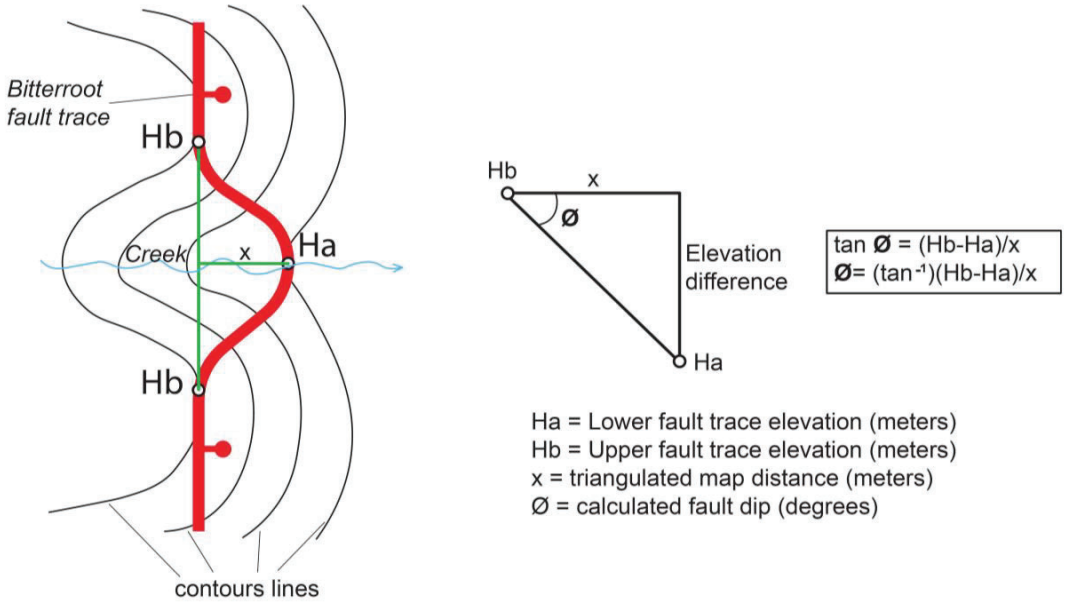

Fault dip calculations using 3-point problem (Method 2): Non-equivalent fault trace elevation across topography.

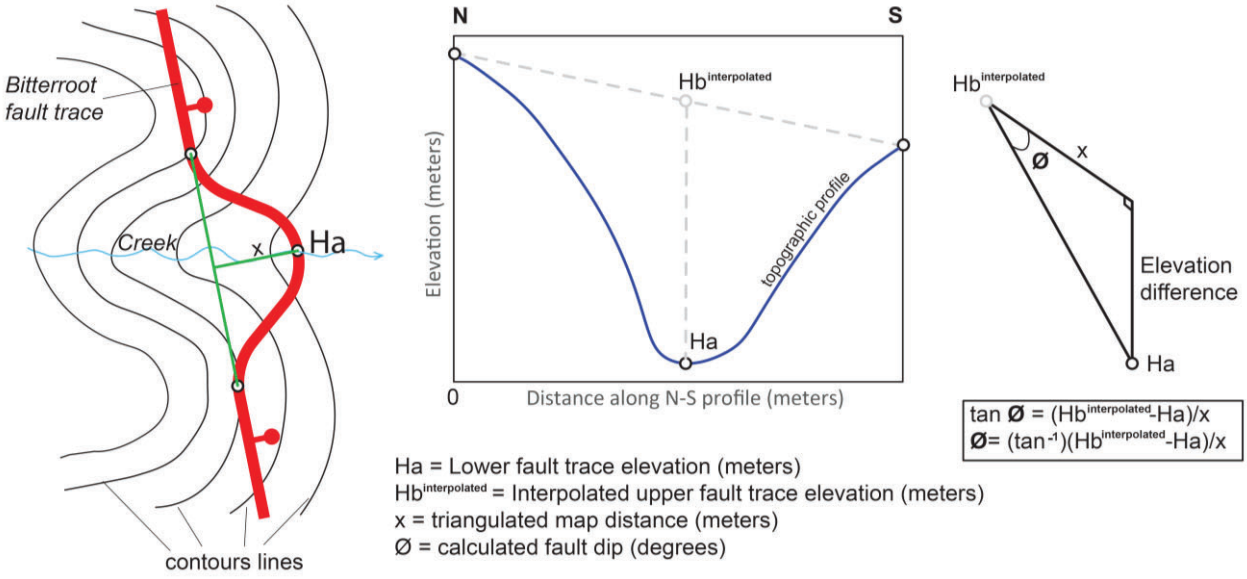

Ha = Lower fault trace elevation (meters)
$Hb^{interpolated}$ = Interpolated upper fault trace elevation (meters)
x = triangulated map distance (meters)
Ø = calculated fault dip (degrees)

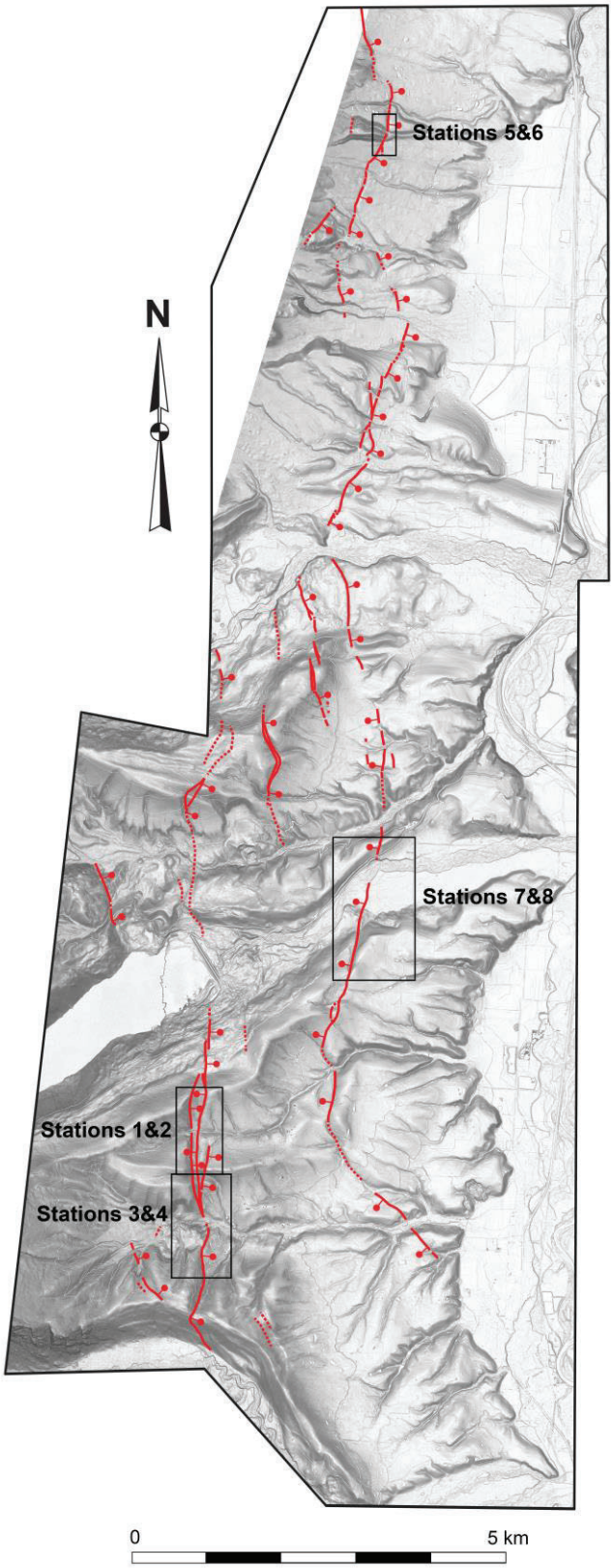

Location of stations 1-8 where fault dips were calculated using 3-point problem methods.

Station 1 (*Como ridges)*

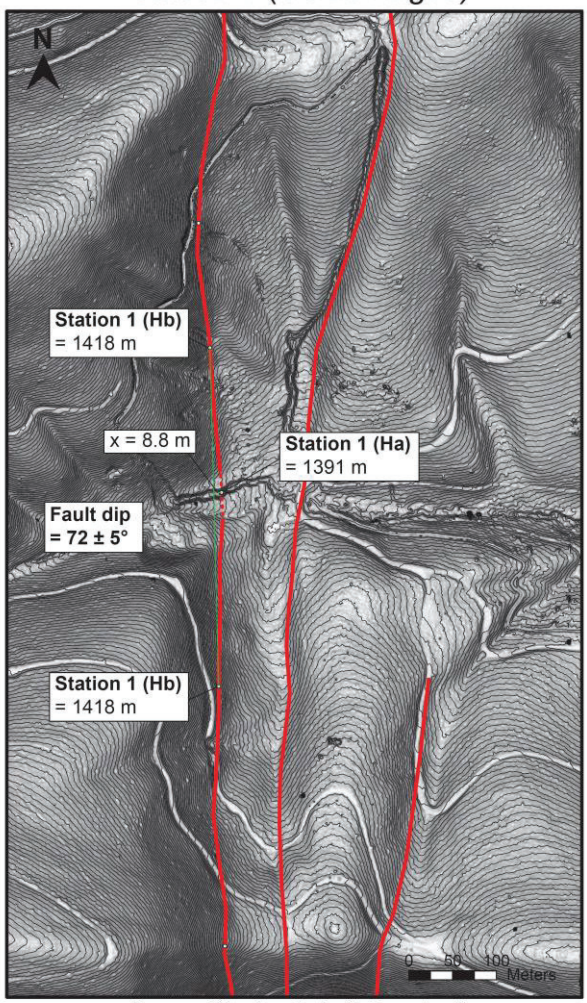

Basemap: Lidar slopeshade with 1m contour lines.

Station 2 (*Como ridges)*

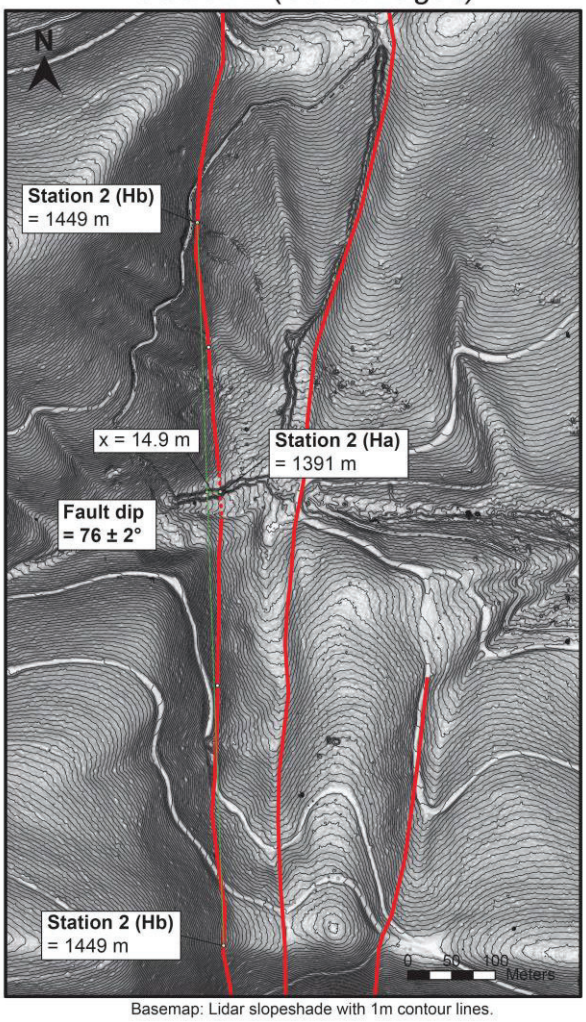

Basemap: Lidar slopeshade with 1m contour lines.

Fault dip calculations using 3-point problem (Method 2): Non-equivalent fault trace elevation across topography.

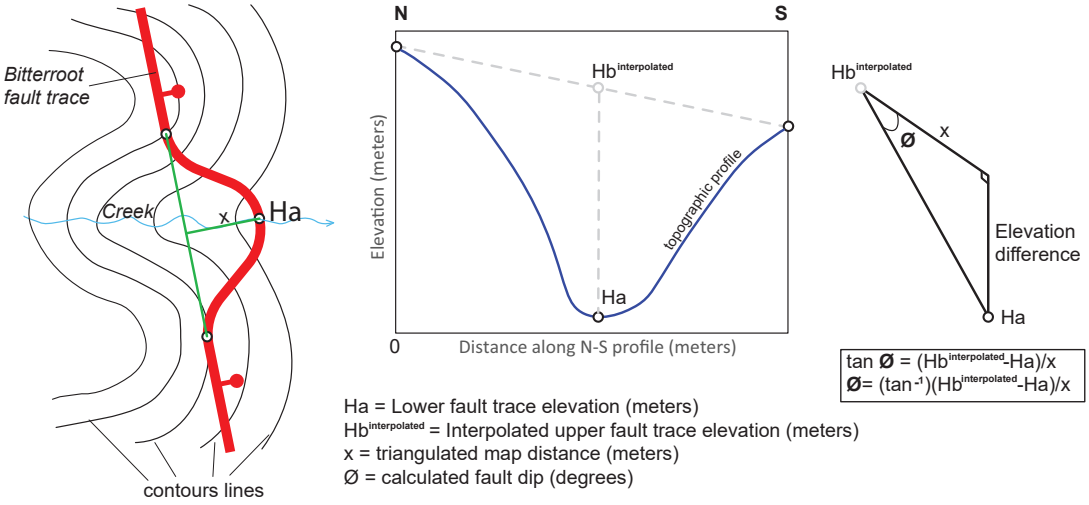

Ha = Lower fault trace elevation (meters)
$Hb^{interpolated}$ = Interpolated upper fault trace elevation (meters)
x = triangulated map distance (meters)
Ø = calculated fault dip (degrees)

Station 3 (*Bunkhouse Creek*)*

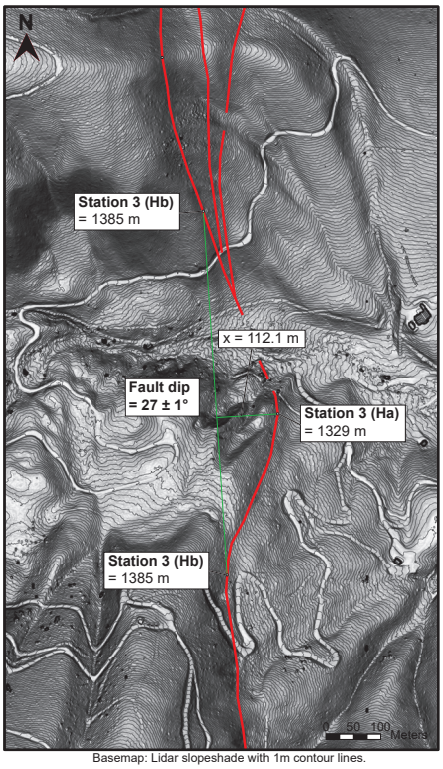

Basemap: Lidar slopeshade with 1m contour lines.

Station 4 (*Bunkhouse Creek*)*

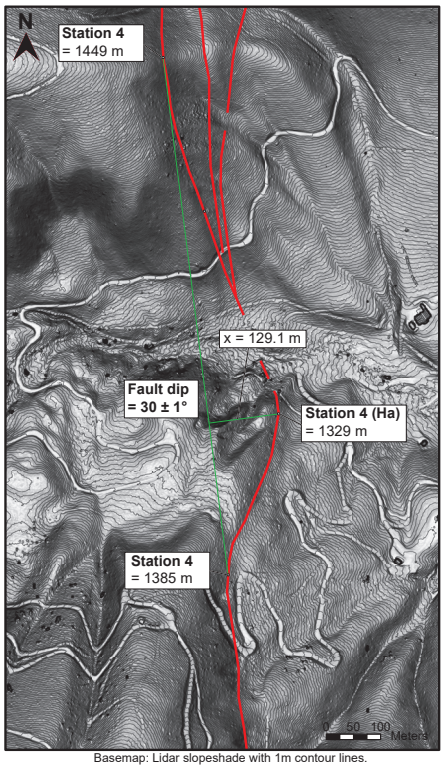

Basemap: Lidar slopeshade with 1m contour lines.

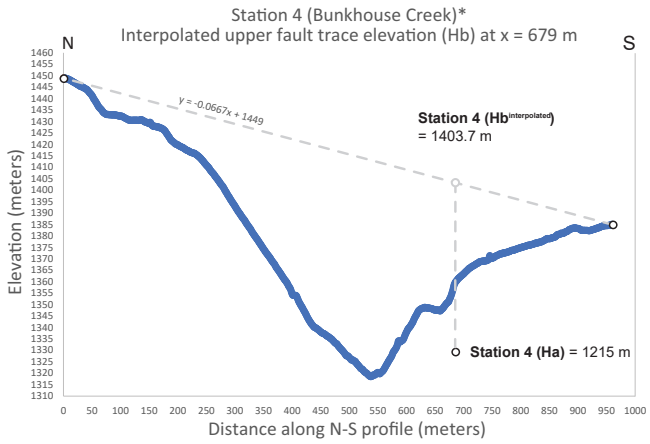

Station 5 (*Ward Creek*)

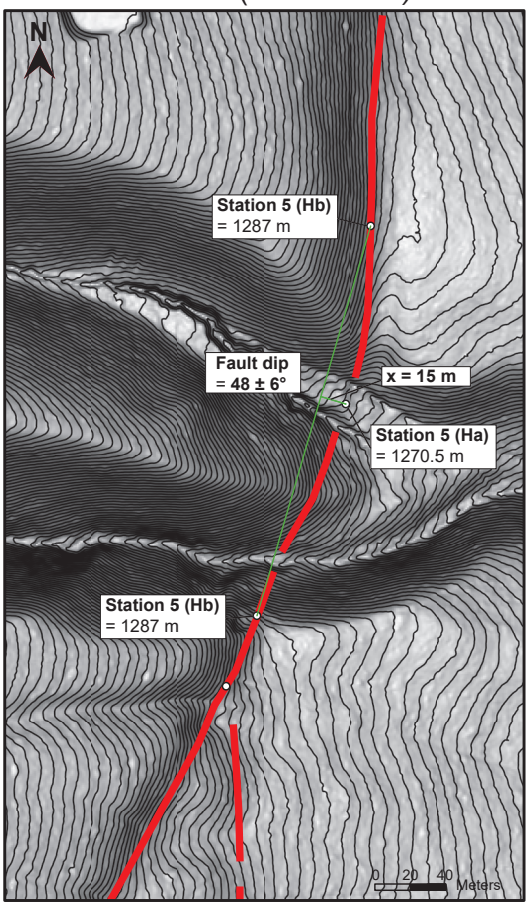

Basemap: Lidar slopeshade with 1m contour lines.

Station 6 (*Ward Creek*)

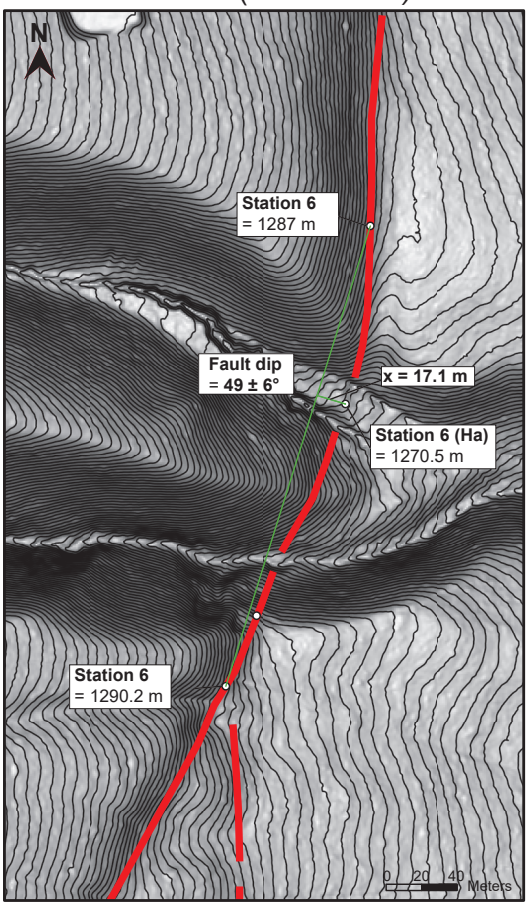

Basemap: Lidar slopeshade with 1m contour lines.

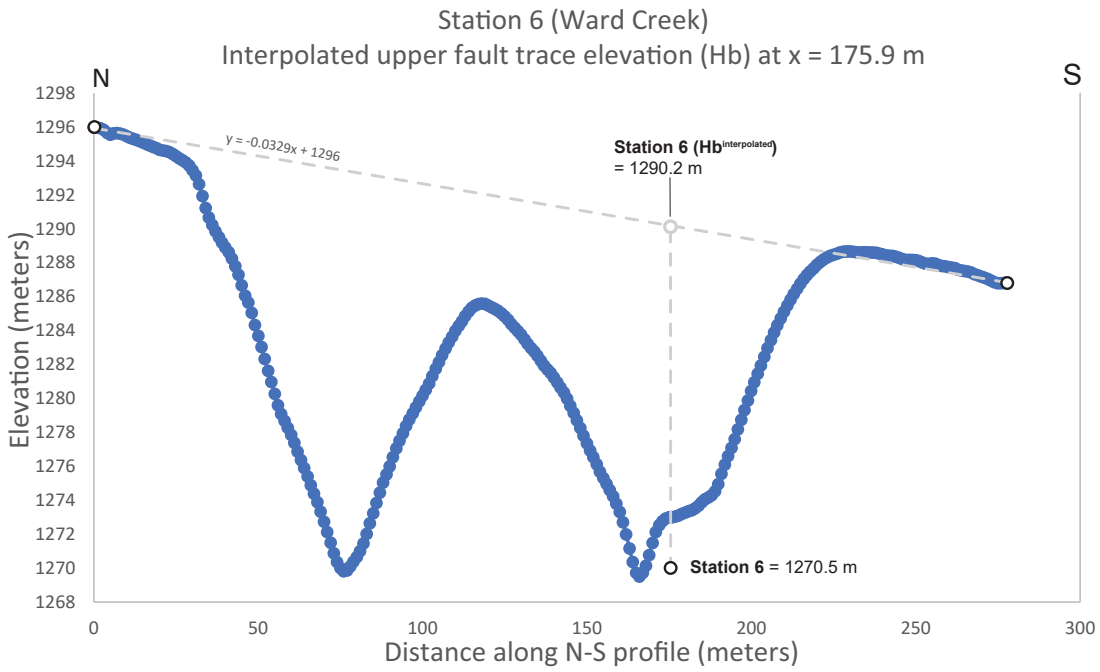

Station 7 (*Rock Creek*)

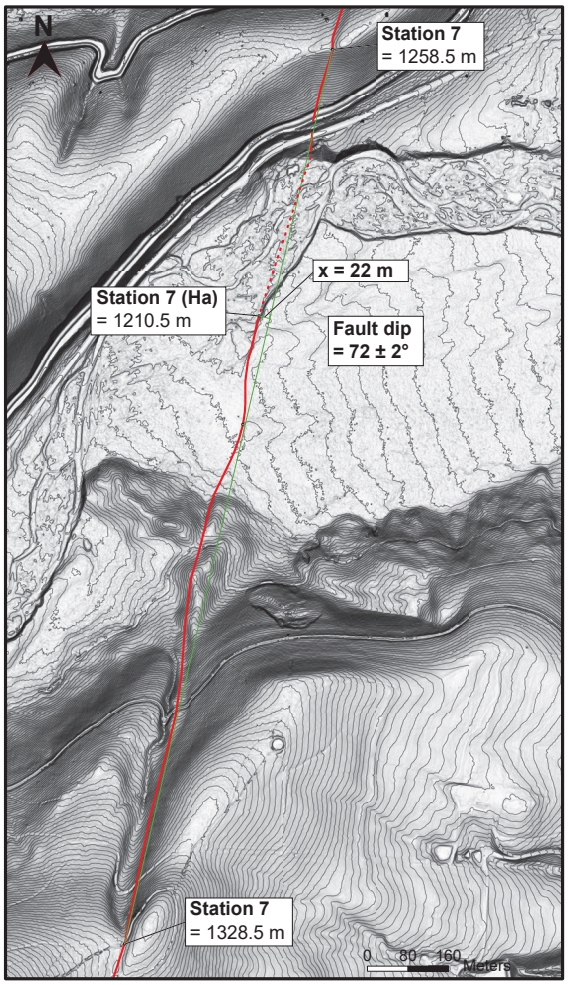

Basemap: Lidar slopeshade with 1m contour lines.

Station 8 (*Rock Creek*)

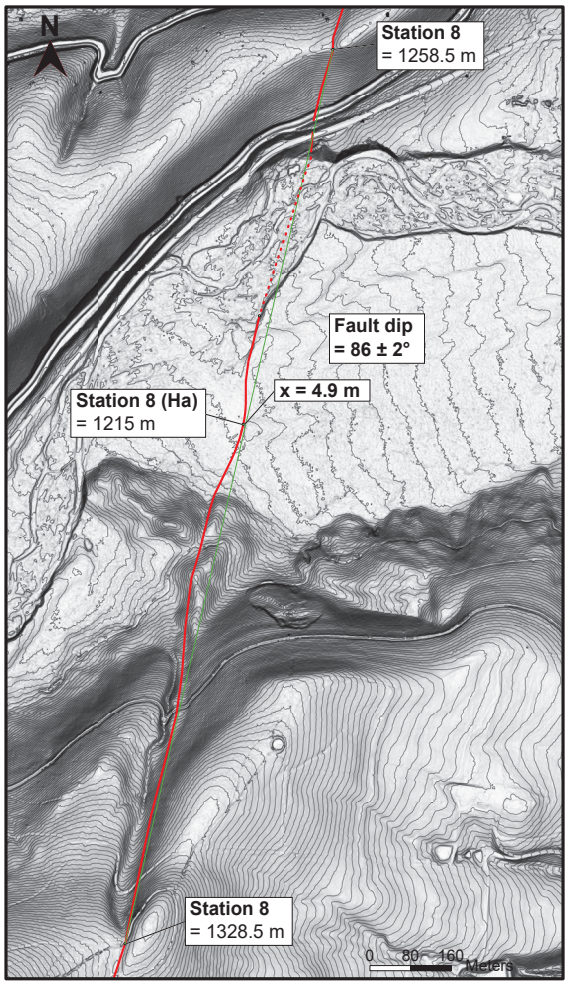

Basemap: Lidar slopeshade with 1m contour lines.